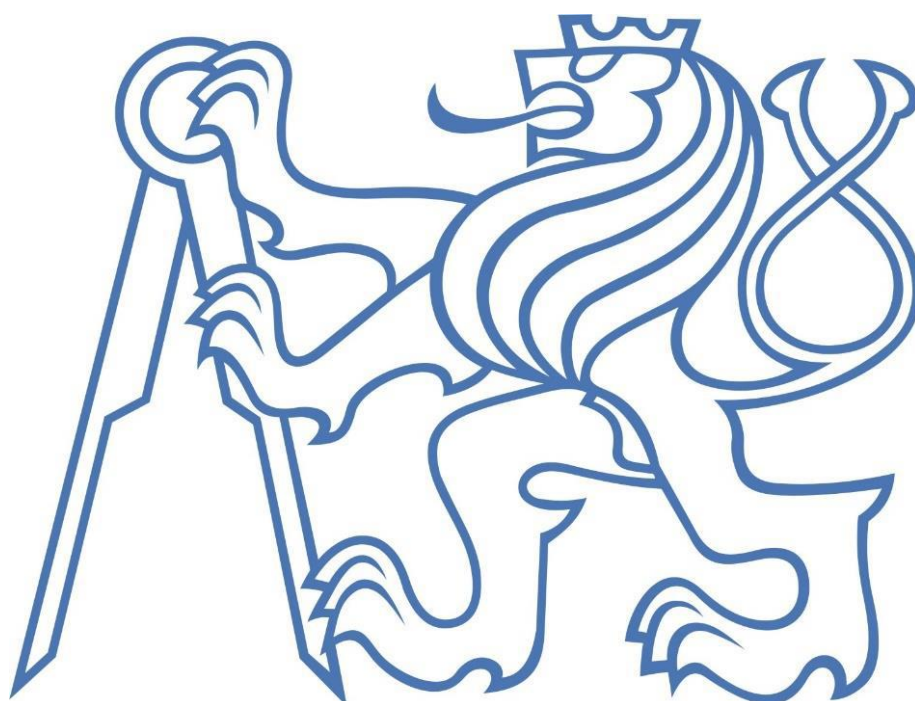


**CZECH TECHNICAL UNIVERSITY IN PRAGUE**



**Doctoral Thesis Statement**



CZECH TECHNICAL UNIVERSITY IN PRAGUE  
Faculty of Biomedical Engineering  
Department of Biomedical Technology

*Josef Soucek*

Magnetic field imaging in biological systems with  
nanometric resolution

Ph.D. Programme: Biomedical and Clinical Technology  
Branch of study: Biomedical and Clinical Technology

Doctoral thesis statement for obtaining the academic  
title „Doctor of Philosophy“, abbreviated to „Ph.D.“

*Kladno, March, 2024*

The work was produced in the bilateral Ph.D. study between the Department of Natural Sciences of the Faculty of Biomedical Engineering of the CTU in Prague, together with Universiteit Hasselt in bilateral cooperation.

**Candidate:** Ing. Josef Soucek  
CTU in Prague, FBE  
Nám. Sítná 3105, 272 01 Kladno, Czech Republic

For faculty of Biomedical Engineering, CTU:

**Supervisor:** Mgr. Zdeněk Remeš, Ph.D.  
Institute of Physics CAS, v. v. i.  
Cukrovarnická 10/112, Prague 6

**Co-supervisor:** Prof. RNDr. Miloš Nesládek, CSc, HDR  
IMEC, Institute for Materials Research, University Hasselt  
Wetenschapspark 1, B-3590 Diepenbeek, Belgium

**Oponents:**

For faculty of Science, UHasselt:

**Supervisor:** Prof. RNDr. Miloš Nesládek, CSc, HDR  
IMEC, Institute for Materials Research, University Hasselt  
Wetenschapspark 1, B-3590 Diepenbeek, Belgium

**Co-supervisor:** Mgr. Zdeněk Remeš, Ph.D.  
Institute of Physics CAS, v. v. i.  
Cukrovarnická 10/112, Prague 6

The Doctoral thesis statement was distributed on .....

The defence of the Doctoral thesis will be held on ..... at  
..... in front of the Board for the Defence of the Doctoral Thesis in the  
Doctoral programme Biomedical and Clinical Technology in the room No.  
..... of the Faculty of Biomedical Engineering of the CTU. Those interested  
may get acquainted with the Doctoral thesis at the Dean Office of the Faculty of  
Biomedical Engineering of the CTU in Prague, Sitna sq., 3105, 272 01 Kladno,  
Czech Republic.

.....  
Prof. Ing. Karel Roubík, Ph.D.  
Chair of the Board for the Defence of the Doctoral Thesis  
in the branch of study Biomedical and Clinical Technology  
Faculty of Biomedical Engineering of the CTU in Prague  
Sitna sq., 3105, 272 01 Kladno, Czech Republic

## Table of contents

1.	Introduction.....	1
1.1	Aim of thesis.....	2
2.	State of art.....	3
2.1	Nitrogen-vacancy.....	3
2.2	Readout techniques.....	4
2.3	Applications.....	5
3	Methods.....	7
3.1	NV defect model.....	7
3.2	Model of crystal environment.....	8
3.3	Chip design.....	8
3.3.1	Chip for single crystal diamond.....	9
3.3.2	Chip for ND.....	11
3.4	Diamond and cell material.....	12
4	Results.....	13
4.1	NV defect results.....	13
4.1.1	Time simulation.....	14
4.1.2	Laser power-dependent simulation.....	14
4.1.3	Relaxation rates discussion.....	15
4.2	Influence of environment on spin contrast.....	16
4.2.1	Effect of Ns centre.....	16
4.2.2	Effect of acceptor level (level X).....	19
4.2.3	Signal volume generation.....	<b>Chyba! Záložka není definována.</b>
4.3	Chip testing.....	22
4.3.1	Chip for single crystal diamond.....	22
4.3.2	Chip for NDs.....	26
5	Conclusion.....	30
5.1	NV defect model.....	31
5.2	Influence of the environment on spin contrast.....	31
5.3	Chip design and testing.....	32
	References.....	33
	Author relevant publications.....	39
	Summary.....	40

# 1. Introduction

This thesis is aimed at developing the concept of a quantum chip for sensing physical fields such as magnetic field ( $\sim 10\text{fT}$ ) and temperature field in nanometric resolution based on sensing the NV spin system. The concept is focused on the optical and photoelectrical readout of a signal [1]. Modelling of this photoelectrical readout is challenging, in comparison with optical readout, because the charge dynamics and excitation and recombination processes in conduction and valence bands need to be introduced. The full quantum mechanical model is essential for further chip development. This requires the implementation of intraband and outerband transition that will allow us to predict the behaviour of the quantum NV chip for different kinds of laser and microwave stimulation and its reaction to the environment. All these features will lead to the characterization of the physical behaviour of the NV defect and point to the essential requirements for further chip design. The model can generally be used for all kinds of diamond-based sensors based upon an NV center point defect. (nanodiamond particles (ND), diamond layers or diamond bulks). Various possible chip designs will be created and modelled in terms of the theoretical quality of the generated signal. The fabricated quantum sensor prototype will be later tested in terms of signal quality and excitation ability in the selected biological environments.

Nanodiamonds containing the NV centres present a promising candidate for biosensing and bioimaging within biological systems, owing to their inherent biocompatibility, non-toxicity, photostability and possible particle size  $>5\text{nm}$ . The small particle size holds significant importance in the uptake mechanism, wherein smaller dimensions enhance endosomal penetration. Leveraging the quantum sensing capabilities of the NDs offers opportunities to monitor weak magnetic or temperature fields in biological processes.

The detection of ultra-low magnetic fields generated within living organisms represents a compelling avenue for extracting valuable insights into biological processes. Such fields are perceptible across diverse anatomical regions and are scrutinized through various clinical methodologies, including neuromagnetography, magnetocardiography, and magnetogastrography. Contrary to electric fields, which strongly depend on the dielectric properties of the tissue between neuronal sources and the recording electrode, magnetic fields travel through tissue without distortion because the respective permeability is essentially the same as free space. NV centre quantum spin states are sensitive to the low fields, and thanks to the fact that sensing doesn't require cooling and can be done at room temperature, it makes it possible to use diamond-based sensors inside *in vitro* or even *in vivo* sensing.

Increasing the local temperature around the eukaryotic cells can be linked to the opening/closing of the temperature-sensitive ion channel of the transient receptor potential channel (TRP) [2]. For measuring the local temperature that is affecting TRP channels, it is necessary to have the sensing tool in proximity to the receptor itself, which is a challenge in itself. Until now, there has been no study that links the activation of the TRP receptors and the local temperature. The current approach is limited to the single-pointed heated element. However, this technique leads to multiple artefacts, including the destruction of many cells, which sets free a multitude of toxic intracellular components, leading to a microenvironment with no resemblance to the physiological situation. Designed chips incorporating microwave and laser heating should avoid this situation, thereby enabling precise sensing utilising nanodiamonds. This approach affords the unique capability to monitor temperature gradients alongside magnetic field variations within the immediate vicinity of cellular membranes.

## 1.1 Aim of thesis

The objective of this thesis was obtained through the implementation of these methodical procedures:

### 1. NV defect modelling

A full mathematical model of the NV defect will be developed based on the rate equation description and theoretical output signal, and its dependency on laser and microwave stimulation will be probed.

### 2. Crystal environment modelling

The effect of the crystal environment will be probed, different common diamond impurities (f.e. substitutional nitrogen,  $N_s$ ) will be added, and their recombination dynamics will be added. Fulfilling this goal requires the implementation of valence and conduction bands with the charge carrier drift implementation so that charge carriers can interact with the other defects.

### 3. Experimental verification

A predicted signal output from the model will be compared with the real measurements on the single NV diamond sample. This goal will be used to validate the proposed physical model.

### 4. Chip designing and manufacturing.

Multiple sensor designs (a combination of PCB and electrodes) will be proposed for the single crystal and nanodiamond applications. Designs will be developed in terms of the minimalization of crosstalk between the MW line and the electrodes, the optimisation of S parameters, and the direct impact on the NV signal. A prototype of the chips will be manufactured using the crystal and electrode preparation process.

### 5. Chip testing on fantoms

Sensor prototypes with the diamond crystals will be tested for elementary characteristics like electrode pickup or S parameters. The results will be compared with the currently used sensors.

### 6. Chip testing on the biological environment

Sensors developed for the NDs application will be tested for temperature and magnetic field sensing in vitro in the real biological system (NDs will be attached to the neuron axons). The concept of using the NV as a multisensor for quantum detection will be shown.

## 2. State of art

### 2.1 Nitrogen-vacancy

The nitrogen vacancy (NV) center is a crystallographic point defect in the diamond lattice. It is formed when one of the four carbon atoms is replaced by nitrogen (N), and the second one is replaced by an empty space (vacancy - V). The NV defect has trigonal symmetry  $C_{3v}$ . Nitrogen is an element from group V in the periodic table, so it has five valence electrons. Three of them are bonded to the neighbouring carbon atoms; two remain free and form a lone-pair orbital, which then interacts with the two free electrons from the carbon lattice induced by the vacancy. Two main charge states of this defect, neutral  $NV^0$  and negative  $NV^-$ , are known from spectroscopic studies using optical absorption [3, 4], photoluminescence (PL) [5], electron paramagnetic resonance (EPR) [6–8] and optically detected magnetic resonance (ODMR) [9], which can be viewed as a hybrid of PL and EPR; most details of the structure originate from EPR. Figure 1A shows the electronic structure of the  $NV^-$  charge state. Electronic structure consist of the ground triplet state (GS), excited triplet state (ES) and the metastable singlet state. The energy distance between the GS and the ES is 1.945eV (zero phonon line (ZPL) is 637nm). Figure 1A shows the fine structure of GS, the energy difference between  $m_s=0$  state and degenerate  $m_s=\pm 1$  state is equal to  $D_{GS}=2.87\text{GHz}$ . Under **external magnetic field** degenerate  $m_s=\pm 1$  state starts split to  $m_s=+1$  state and  $m_s=-1$  state (**Zeeman splitting**, Figure 1B) and value of the splitting can be estimated to  $28\text{MHz/mT}$ . This system can detect very weak magnetic field in order of nT or lower [10]. Parameter  $D_{GS}$  stays for the axial Zero Field Splitting (ZFS) parameter that was estimated at a value of  $2.87\text{GHz}$  at room temperature [11].

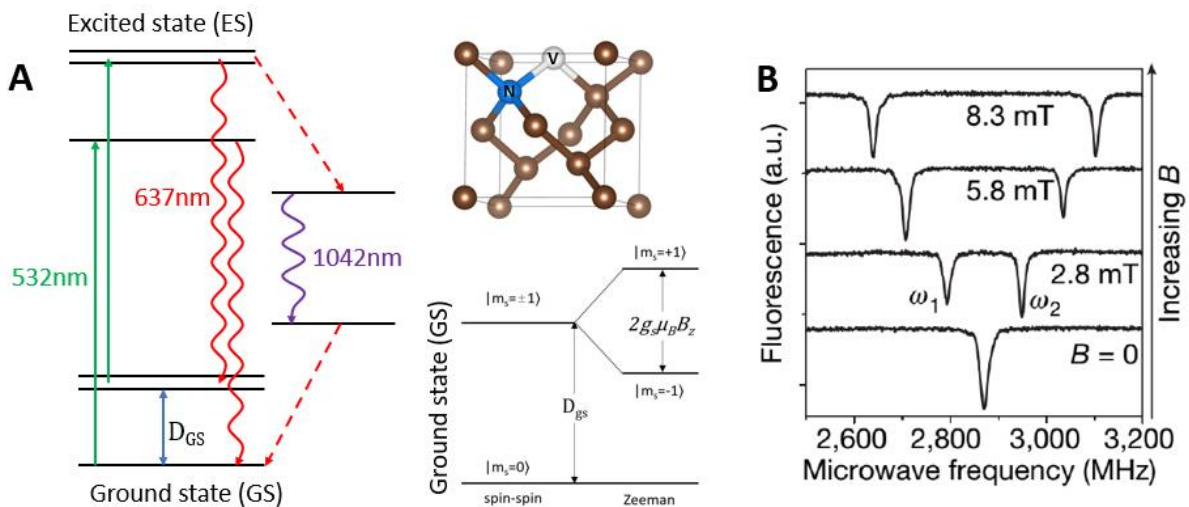


Figure 1 – A: Energy diagram of the NV centre, with sketch of the ground state with split of degenerate state  $m_s=\pm 1$  (Zeeman split) that is proportional to the external magnetic field  $B_z$  ( $g_s$  stands for electron spin factor,  $\mu_b$  stands for Bohr magnetron). B: ODMR spectra of the NV center for different values of external magnetic field 8.3, 5.8, 2.8 and 0mT. Drop in fluorescence at frequency  $\omega_1$  stays for transition  $|m_s=0\rangle \rightarrow |m_s=-1\rangle$ ,  $\omega_2$  between the  $|m_s=0\rangle \rightarrow |m_s=+1\rangle$  [12]

The shift of the value of the  $D_{GS}$  can be used for the calculation of the **local temperature**. This effect is expected due to the spin-spin coupling between two unpairing electrons forming the center [13]. The estimated thermal shift of the  $D_{GS}$  parameter from a calculation from *an initio* values [14] and the experimental [15] measurements gives us a value of  $-74.2\text{ kHz/K}$ . The temperature shift effect in energy level position and ODMR spectra is depicted in Figure 2.

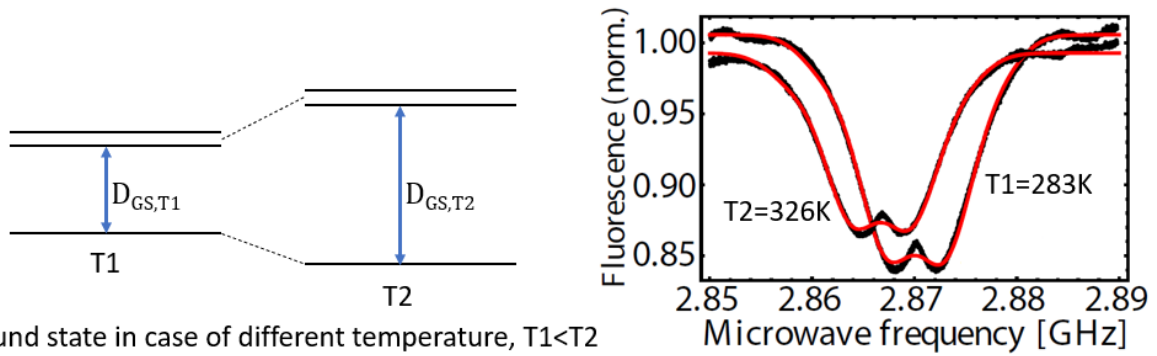


Figure 2 - A: Graphical representation of changing of DGS parameter for the two different temperatures  $T_1$  and  $T_2$ , B: shows the shift in the normalized ODMR spectra for two different temperatures  $T_1=283\text{K}$ ,  $T_2=326\text{K}$ . A: visualised by author, B: taken and modified from [15]

The external field magnetic field caused the Zeeman effect, leading to the separation of the  $m_s=\pm 1$  to the two levels  $m_s=+1$  and  $m_s=-1$ . When the field  $B_z=\pm 102.4\text{mT}$  energy level  $m_s=-1$  degenerates with the energy level  $m_s=0$  and creates a mixed state, causing a sharp drop in the fluorescence spectra, indicates Ground State Level Anti Crossing (**GSLAC**). This microwave free method improves the fidelity of the classical readout methods by  $\sqrt{3}$  [16]. Schema of the GSLAC and fluorescence spectra are shown in Figure 3. Traces of fluorescence near the GSLAC event show the additional features that can be attributed to the cross-relaxation with the nearby spin bath [17]. GSLAC contrast trace showing narrow magnetic resonance (FWHM  $\approx 38\mu\text{T}$ ) as a function of  $B_z$  field centred around zero transverse field [18].

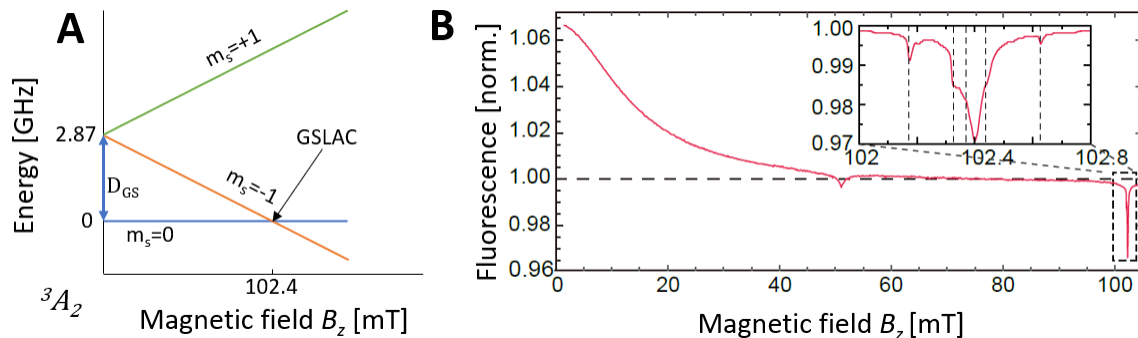


Figure 3 - A: Graphical representation of the Zeeman splitting with GSLAC when the  $B_z$  field is applied. B- shows the fluorescence spectra as a function of applied  $B_z$  with the sharp drop in fluorescence intensity at  $102.4\text{mT}$  caused by GSLAC. Taken and modified from [18]

## 2.2 Readout techniques

Continuous-wave optically detected resonance (**CW-ODMR**) is a simple and widely used ESR method. In the CW method, the optical excitation, the MW spin driving, and the photon readout occur continuously and simultaneously. The laser excitation of the NV center transfers electrons to the higher excited state, from which they recombine either radiatively or non-radiatively and end up in the  $m_s=0$  state. It is called spin polarization. The laser light then continuously polarizes the NV<sup>-</sup> ground state  $m_s=0$  (GSO, bright state), MW near-resonant frequency drives the population to ground state  $\pm 1$  (GS $\pm 1$ ). From this sublevel, the electron is excited to the  $m_s=+1$  excited state, and it returns to the ground state with 70% radiatively and 30% non-radiatively (dark transition). The ratio between the bright and the dark transition is called the spin contrast. Photoelectric-detected magnetic resonance (**PDMR**) has been developed jointly in the last decade for the detection of ESR by UHasselt and CTU

(Prof. Nesladek's group). The principle of this method is that an electron can be promoted from ES to CB by two-photon ionization (one photon is required for the excitation electron to the excited state, and the second photon is required for the excitation from ES to CB). In this process,  $NV^-$  loses one electron and becomes  $NV^0$ . This system can be reinitialized by pumping the electron from VB to  $NV^0$ , and then  $NV^0$  is transformed back into  $NV^-$ . This process is called back conversion. These charge carriers are transported under a bias voltage to the collecting electrodes. Unlike ODMR, the PDMR requires a diamond sample to be electrically connected. Figure 4 shows one possible chip for the PDMR readout. Electrodes are fabricated on the diamond surface by a standard lithography technique and are connected to the source of the bias voltage via the SMA ports  $p_3$  and  $p_4$ . The current is measured by a lock-in amplifier. Microwave is connected via port  $p_1$ , and they are terminated at  $p_2$  with a  $50\Omega$  load. PDMR leads to increased detection efficiency, higher spatial resolution, and easier on-chip integration compared to the ODMR technique. The absence of optics for photon collection unlocks the possibility of miniaturizing the quantum chip size (chip size  $\sim 50nm$  can be achieved). [1]

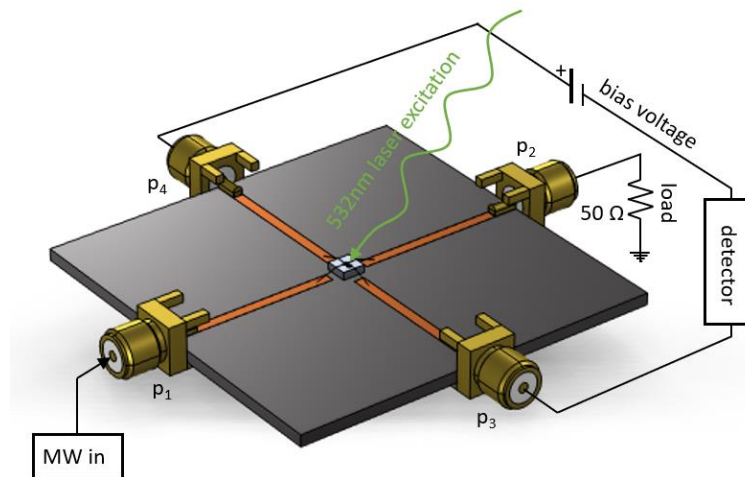


Figure 4 - Schematic representation of chip conformation, PCB with diamond crystal in center excited by 532nm laser,  $p_{1-4}$  stays for SMA port,  $p_1$  is used for MW source,  $p_2$  is connected to  $50\Omega$  terminator,  $p_{4-3}$  is connected to bias voltage and to the detector. Visualized by author.

## 2.3 Applications

One of the widest application fields of diamond-based sensors is the detection of low external magnetic fields. Current magnetometer sensors can achieve few femto Tesla resolutions (f.e. SQUID, SERF), but they need to operate at low temperatures, high vacuum levels, etc.. the NV-diamond sensor can work at pressures to 60GPa [19] and temperatures from cryogenic to 700K [20]. Diamond-based sensors allow sensing signals in DC or AC mode up to 50MHz. Both AC and DC sensitivity are limited by the  $NV^-$  relaxation time [16]. DC sensitivity is limited by the inhomogeneous dephasing time  $T_2^*$  ( $\sim 1\mu s$ ), AC sensitivity is limited by longitudinal relaxation time  $T_1$  and homogeneous spin decoherence time  $T_2$ . Over the past years, various magnetic sensing methods using the NV centers in bulk, at the diamond surface and as well in diamond nanoparticles have been developed. [21]. Various recent studies show the usage of the single NV quantum sensor for the detection of nuclear spins [22],

external single electron spin [23] or the concept of the single molecule 3D nano MRI that uses the quantum imaging technique with the super-resolution [24].

Nanodiamonds containing fluorescent Nitrogen-Vacancy (NV) centres are the smallest single particles, of which, by recording spectral shifts or changes in relaxation rates, various physical and chemical quantities can be measured, such as the magnetic field, orientation, temperature, radical concentration, pH or even NMR. This turns NV-nanodiamonds into nanoscale quantum sensors, which can be read out by a sensitive fluorescence microscope equipped with an additional magnetic resonance upgrade [25]. NDs can be used as the biological marker, quantum sensing or as tool for the targeted drug delivery.

Several studies[26–28] used NDs as fluorescence markers in cells and tissues of different creatures (*Caenorhabditis elegans*, *Escherichia Coli*, *Mus musculus*, *Sus domesticus*). All of the studies showed no photobleaching of NDs. In general, no harmful effect of the NDs on the creatures was observed. The study [27] shows the usage of functionalized NDs for the high-resolution imaging of the tumour morphology over the eight days. Study [28] shows that NDs can be used for quantitative tracking of human MSC beyond the rotten model with single-cell accuracy.

Thanks to the good dispersibility in the water, and the large surface area ND particles are suitable tool for targeted drug therapy. Drugs can be chemically or physically attached to the ND surface by bounding to the functional group at the surface. The principle of the targeted/non-targeted drug delivery (in this case, anti-tumour drug Dox (doxorubicin) is depicted in Figure 5. Most of the studies [29–31] aim to deliver anti-tumour drugs to the tumour cell lines (HeLa, HepG2, MCF-7) with usage of pH-induced target drug delivery system.

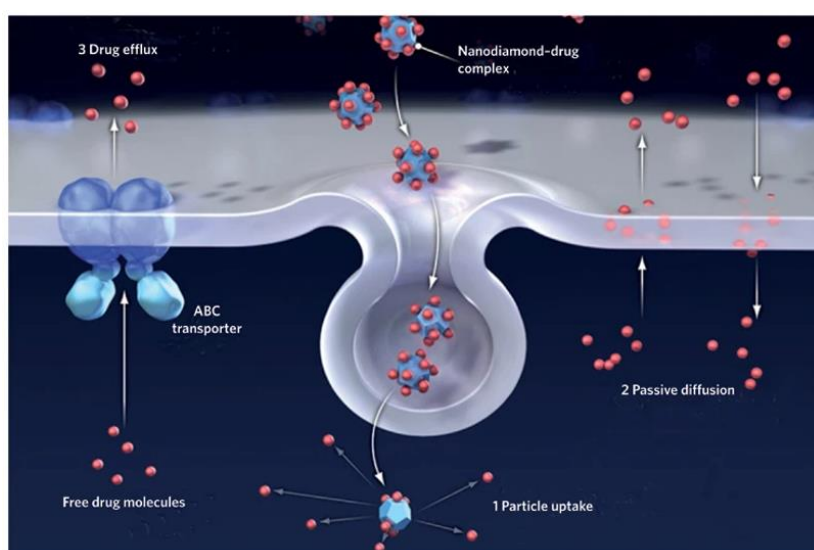


Figure 5 - Schematic representation of transporting of Dox drug to the cell with method 1) NDs-Dox complex via endocytosis. 2. Passive diffusion of Dox via the cell membrane, 3. Transport Dox via the ABC transporter proteins. Taken from [31]

NV-based quantum sensors can also be used to measure precise physical properties like temperature strain or electric fields with nanoscale precision. For temperature, a wide-range temperature sensor (~90K) with a resolution of a few mK was reported [32, 33]. The advantage of the usage of NDs as a temperature probe is the possibility of monitoring the probe's close environment and sub-cellular temperature gradient, which is essential for the understanding of temperature-involved fundamental

functions like the genesis of an action potential or cell metabolism. The first pioneering study that uses NDs as a quantum temperature probe has been published recently [34].

## 3 Methods

### 3.1 NV defect model

Here, we proposed NV defect as a six-energy level system within a one-electron approximation. NV<sup>-</sup> charge state considers five energy levels: The  $m_s=0$  and  $m_s=\pm 1$  for the unsplit ground state (GS) and excited state (ES) triplet states, the metastable-state singlet is approximated by the one energy level since the singlet  $^1A_1$  has a short relaxation time. We consider the presence of zero external magnetic field, which means there is no Zeeman split presented. The NV<sup>0</sup> charge state is presented as a level system (the inner dynamics of the NV<sup>0</sup> are not conceded). Photoionisation is realized from the valence band to the NV<sup>0</sup> charge state by the two-photon process, in this process the extra electron is photoionised to the NV<sup>0</sup> and the defect changes the charge to the NV<sup>-</sup> and a hole charge carrier is produced in the valence band (VB). The electron that is responsible for the charge state transition can end at the GS (with a probability~ 80%) or at the metastable-state singlet (with a probability~ 20%) [35]. The second part of the defect ionisation consists of the excitation of the electron from the GS of the NV<sup>-</sup> to the ES by a single photon, in ES the electron has the possibility to excite the second photon to the conduction band (CB) and NV<sup>-</sup> change the charge state back to the NV<sup>0</sup>. One-photon excitation is the principle of the ODMR signal (low laser power regime), while two-photon ionisation is the principle of the PDMR signal generation (high laser power regime). The process generates the free electron in the CB. If the electron in ES is not excited, the electron will relax by the radiative (emitting fluorescence photon) or non-radiative (via the metastable-singlet) way back to the NV<sup>-</sup> GS. All the possible transitions are shown in Figure 6.

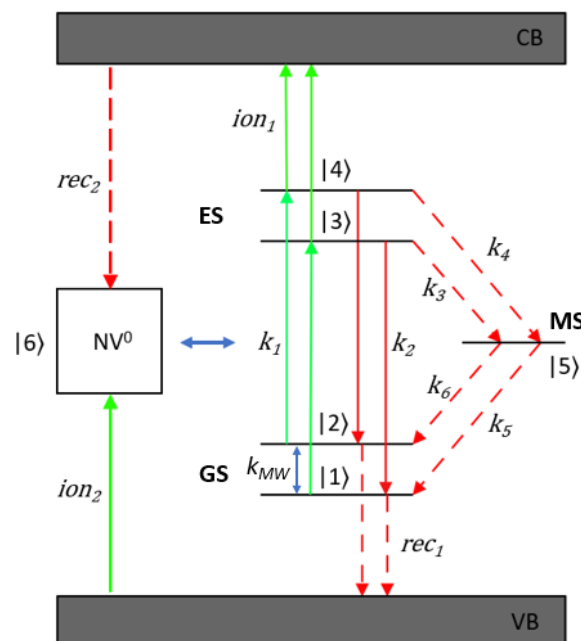


Figure 6 - Energy level system of NV defect. Levels 1-2 represent the GS of NV<sup>-</sup>, 3-4 the ES of NV<sup>-</sup>, 5 the metastable state (MS), 6 denotes the NV<sup>0</sup> charge state, VB denotes the valence band and CB the conduction band. The colour of the arrows defines excitation (green) and relaxation (red). The solid lines relate to ionisation or radiative relaxation, and the dashed lines relate to non-radiative relaxation.  $k_i$  denotes the following transitions between energy levels of NV<sup>-</sup> charge state:  $k_1$  (GS to ES),  $k_2$  (ES to GS),  $k_3$  (ES  $m_s=0$  to MS),  $k_4$  (ES  $m_s=\pm 1$  to MS),  $k_5$  (MS to GS  $m_s=0$ ),  $k_6$  (MS to GS  $m_s=\pm 1$ ).  $ion_1$  denotes the ionisation transition from ES of NV<sup>-</sup> to CB,  $ion_2$  the ionisation transition from VB to NV<sup>0</sup> charge state,  $rec_1$  stands for the recombination

transition between GS of NV<sup>-</sup> and VB,  $rec_2$  for the recombination transition between the CB and NV<sup>0</sup>,  $k_{mw}$  stays for the microwave transition between the energy levels ( $m_s=0$ ,  $m_s=\pm 1$ ) of the GS.

### 3.2 Model of crystal environment

Diamond crystals contain several types of point defects that have a significant effect on the photoelectrically detected signal. To address the full picture of the PDMR method, it is necessary to include this type of defect in the numerical model. N<sub>s</sub> plays a significant role in photocurrent detection through the recombination and trapping processes. Characterisation of the N<sub>s</sub> dynamic is crucial for the full understanding of photocurrent generation. In the PDMR N<sub>s</sub>, photoionisation can cause a decrease in photocurrent, reducing the recombination lifetime of charge carriers and decreasing photoelectrically detected spin-contrast [36–38]. We considered N<sub>s</sub> as one energy level system (Figure 7A) with the two possible charge states, N<sub>s</sub><sup>0</sup>, that after photoionisation became N<sub>s</sub><sup>+</sup>. Consequently, the photo-induced back conversion from N<sub>s</sub><sup>+</sup> to N<sub>s</sub><sup>0</sup> is not possible under the 532nm illumination. The N<sub>s</sub><sup>+</sup> can be back-converted to the N<sub>s</sub><sup>0</sup> by the recombination of the N<sub>s</sub><sup>+</sup> with the free electron from the conduction band. Recently, our experimental results suggested the existence of such an acceptor level [39]. This defect level (noted level X) has the ability to trap an electron or to serve as a recombination centrum (as depicted in Figure 7B) [39, 40]. We found earlier that the presence of acceptor defects could lead to intriguing behaviour, such as the inversion in the sign of the PDMR contrast [39]. In [39] we tentatively attribute this level to the single vacancy V. Acceptor defect X, represented as a one-level system with charge states X<sup>0</sup> and X<sup>+</sup> (Figure 7B). We consider that the charge state transition from X<sup>0</sup> to X<sup>+</sup> by the excitation of the electron from the defect to the CB is not possible.

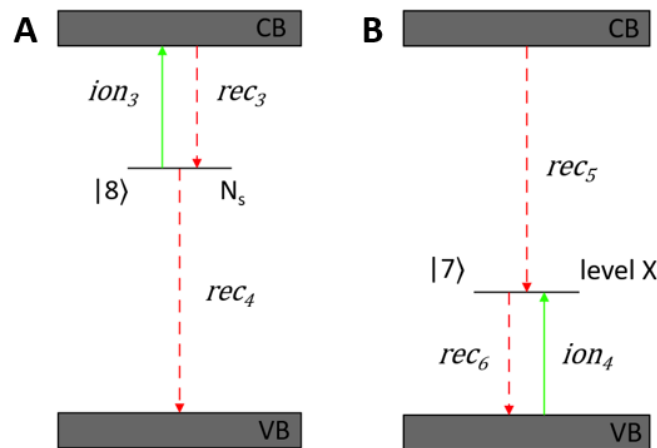


Figure 7 – The proposed structure of the N<sub>s</sub> (A) and acceptor level X (B). A: Defect N<sub>s</sub> is considered as one energy level system |8> with recombination rates  $rec_3$  and  $rec_4$  and ionisation rate  $ion_3$ . B: Defect X is designed as a strong hole producer; rate  $rec_5$  is the recombination rate from the Conduction band (CB) to X<sup>+</sup>,  $rec_6$  is the rate of recombination of X<sup>0</sup> electron to the valence band (VB), rate  $ion_4$  is the ionisation rate from VB to X<sup>+</sup>. This ionisation process leads to the production of holes in the VB.

### 3.3 Chip design

Two chip variants were developed depending on the area of application. One is for the single crystal diamond, and the second is for the nanodiamond (NDs) application.

### 3.3.1 Chip for single crystal diamond

The chip that utilises a single crystal diamond configuration is designed primarily for photoelectrical readout applications but also allows the photoluminescence readout. The design is conceived to ensure uniform excitation of the microwave field across both the crystal volume and frequency spectrum. The magnetic component of the microwave field is oriented perpendicular to the z-axis of the model. Electric tracks that conduct the charge carriers towards electrodes, are shielded by two ground planes, providing minimalization of the electrostatic environmental interference.

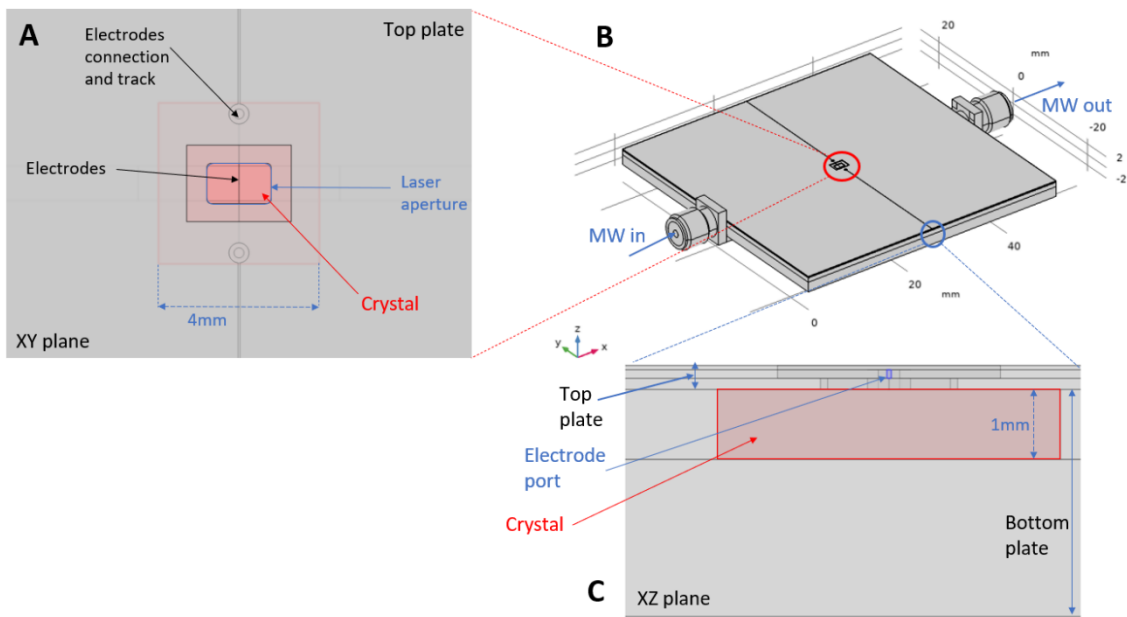


Figure 8 - Modelled chip for single crystal diamond. A: shows the magnification of the laser aperture at the 'top' plate at XY plane. The red rectangle represents the diamond crystal, which is 4x4mm in size, between the chip plates. At the surface of the crystal, a black line representing the electrodes can be seen. Electrodes are connected to the electric tracks via. B: shows the complete plate with the SMA ports dedicated for MW stimulation. C: Shows the magnified XZ plane of the chip with 'top' and 'bottom' plates. The blue area stays for the simple port of the electrode line, and the red box stays for the diamond crystal.

In the simulation, we model the electrodes as 2D planar structures (Figure 9A) oriented perpendicular to the microwave excitation line, utilising the 'Transition boundary condition' with a thickness of 120nm. This approximation closely mimics the behaviour of real sputtered electrodes. Electrodes are fabricated to the crystal surface using the standard lithography procedures. Sputtering is performed within a two-target system, employing targets composed of titanium (Ti) and gold (Au) targets. The resulting electrode structure consists of 20nm of titanium followed by 100nm of gold (Figure 9B).

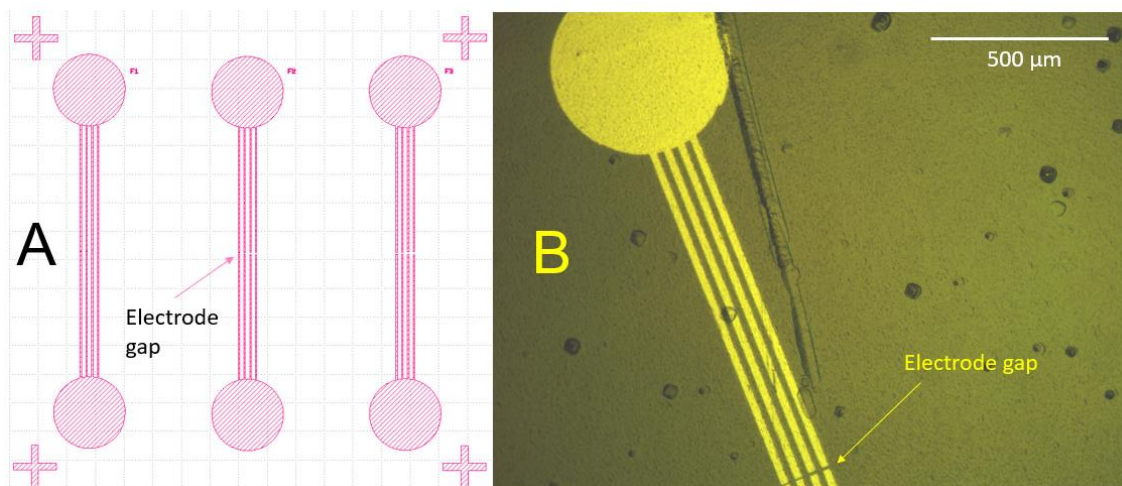


Figure 9 - A: Design of electrode mask for the lithography, electrodes contain multiple tracks to cover the bigger surface of the diamond crystal, and aligning crosses helps position the crystal. B: Image of fabricated electrode structure at the diamond surface

In the second iteration of the prototype (Figure 10), we rectified the errors identified in the initial production phase. Additionally, we augmented functionality by incorporating two pairs of electrodes to extend coverage over the diamond surface. This enhancement not only expands measurement capabilities but also can serve us with a multipixel sensor, unlocking the possibility of sensing, e.g., the gradient of the magnetic field.

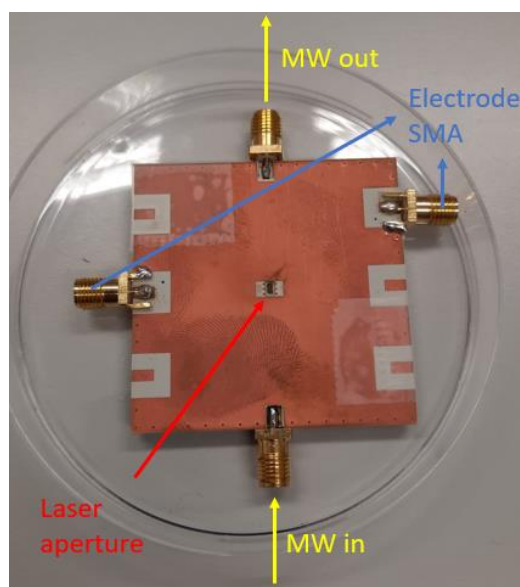


Figure 10 – Second iteration of the chip for single crystal diamond. Microwave features are marked by a yellow color, electrode features a blue color and laser-related features with red colour.

## Chip for single crystal diamond, QNMR variation

A potential application of single crystal diamond is the detection of NMR signals from very small amount of analytes (attolitre – picolitre) i.e. mass-limited samples. In conventional high-field NMR setups, the signal-to-noise ratio (SNR) changes linearly by the volume of the sample [41]. Although

they work quite well for micro-litre samples, they fail at nano and pico-litre scales. However, single crystal diamonds are a promising platform for detecting MR signals from such small-volume samples [42]. We explore the utilisation of a proposed chip as a promising tool for constructing microfluidic chambers. In our experimental setup, we fabricate a microfluidic channel sealed with a transparent glass plate covered with copper tape, serving as the ground plane. The initial prototype undergoes modifications and testing to evaluate its microfluidic properties, such as pressure and flow dynamics, as well as their compatibility with pulsed protocols, including Rabi, Ramsay and Hans-Echo sequences. **Chyba! Nenalezen zdroj odkazů.** shows the adaptation of the Quantum Nuclear Magnetic Resonance (QNMR) chip for incorporating a single crystal diamond membrane with a thickness of 50 $\mu\text{m}$ . An alumina piece is securely affixed to the ground plane of the sensor chip atop the chip. The microfluidic channel is crafted by drilling through both the alumina block and sensor chip, subsequently sealed with a 0.5mm thick glass slide. The diamond membrane is then positioned within the microfluidic channel. Connection to the external microfluidic part is facilitated by  $\frac{1}{4}$ -28 superflangless male nuts. Additionally, the entire bottom surface, except the laser aperture, is covered with black tape to mitigate the multi-reflection of the sensing laser, thereby ensuring operator safety and minimising reflection to the photodiode detector placed near the microfluidic chip. In this microfluidic configuration, we could achieve a flow rate of up to 400  $\mu\text{L/s}$ .

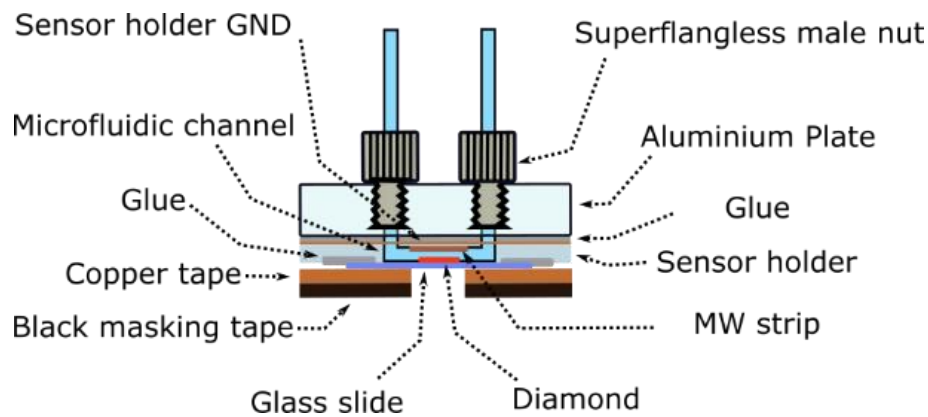


Figure 11 – Chip modification for microfluidic QNMR. A microfluidic channel is placed through the aluminium sensor chip, sealed with the glass plate. Copper tape serves as the ground plane, and masking tape reduces the laser reflection.

### 3.3.2 Chip for ND

The chip that is used for signal detection from the diamond nanoparticles is designed for optical readout applications. In this proposed chip, the microwave stimulation structure has been designed in the shape of an omega, featuring the drilled hole inside the omega structure that serves as a place for placement of the liquid neuron imaging media containing NDs. The omega-shaped structure has an inner diameter of 4.5mm. Notably, the chip incorporates a single electrical pathway equipped with two SMA ports dedicated to microwave stimulation, but the circuit for the photocurrent readout is not presented. The frequency-dependent dielectric properties of the imaging media were determined through the application of a 4-pole Cole-Cole model [43]. Furthermore, a chip has been designed for optical readout detection.

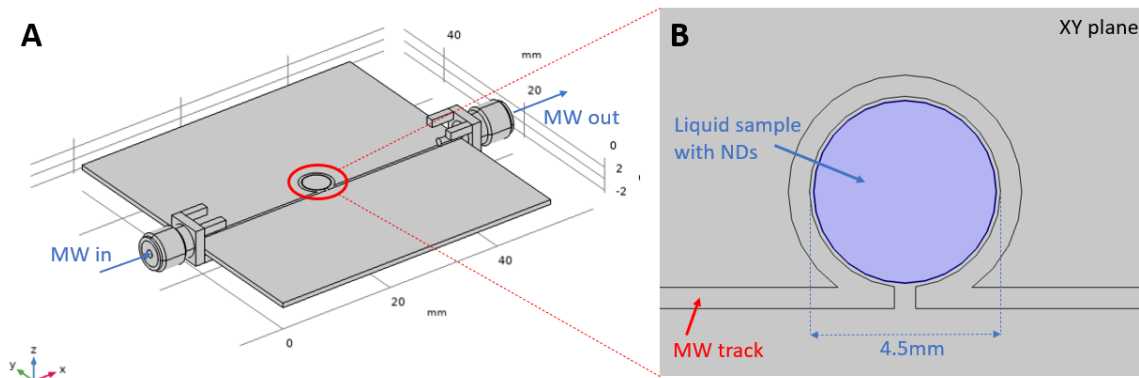


Figure 12 – Modelled chip for the NDs application. A: shows the complete plate with two SMA ports dedicated to the microwave stimulation line. B: shows the magnification of the omega feature in the XY plane. The blue area represents the liquid medium with the NDs that are used for sensing.

Figure 13 shows the fabricated omega-shaped chip that is ready for ND imaging. Before doing so, the cover slip needs to be attached to the chip surface, and the created cavity needs to be filled with the liquid sample that contains the ND particles.

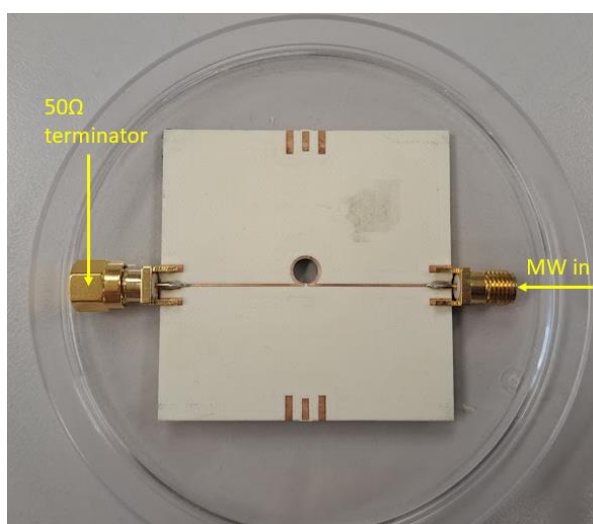


Figure 13 – Fabricated chip for nanodiamond application. Two MW SMA ports are soldered to the conductive tracks. One port serves as the feed of the microwave, while the second port accommodates a 50Ω terminator.

### 3.4 Diamond and cell material

#### Single crystal diamond:

For chapter 4.1 and 4.2.1, we used a single type IIa crystal diamond from the NDT (New Diamond Technology) company. by HPHT method with 3x3x0.5mm ( $\pm 0.05$ mm) size and {1,1,1} face orientation. Surface roughness was approximately 5nm. Notably, the concentration of the impurities was approximately 50 ppb for Boron and 10 ppb for Nitrogen.

In chapter 4.2.2, we used a single type IIa optical grade CVD diamond with  $N_s^0$  concentration less than 1ppm. Sample was electron-irradiated (14 MeV,  $10^{16} \text{ cm}^{-2}$ ) and annealed (700 °C, 4h). Sample contain ~10ppb of bulk NV ensembles.

In chapter 4.2.3., we used a single-crystal {1,1,1} with size 2.1x2.3x0.65 mm diamond, synthesized using a high-temperature high-pressure (HPHT) method. The initial nitrogen concentration of the sample was specified as <200 ppm. To produce NV centers, the sample was electron-irradiated at 14MeV (dose:  $10^{18} \text{ cm}^{-2}$ ) and then annealed at 700 °C for three hours. The resulting NV centers are randomly oriented along all four {1,1,1} crystallographic axes of the diamond.

In chapter 4.3.1. we used a Ib single-crystal diamond {1,0,0} with size 2x1mm with thickness of 35  $\mu\text{m}$ . Sample contain 14ppm of  $N_s$  with the 2ppm of NV.

**Nanodiamond particles:** are sourced from Microdiamant Switzerland were utilized in this work. These particles possess a size median of 0.125 $\mu\text{m}$  with a moderate distribution of 0.105-0.145 $\mu\text{m}$  and contain 100-200 ppm of nitrogen impurities. Monodisperse particles were irradiated at 870 °C within an external target for a duration of 80 hours using a 15.7 eV electron beam, with particle flux of  $2.5 \cdot 10^{19}$  per square centimetre, extracted from the MT-25 microtron. Following irradiation, the NDs underwent annealing at 900 °C for 1 hour under an argon atmosphere, followed by oxidation in the air for 5 hours at 510 °C, yielding final NDs with NV centres.

**Cells:** All experimental procedures were conducted according to the protocol approved by the Institutional Animal Care and Use Committee. Primary cortical neurons were isolated from postnatal day 0 to day 2 (P0-P2) mouse pups. The cortical tissues were dissected, cleaned of the meningeal layer, and then dissociated. First, enzymatically (1% trypsin and 0.1% DNase I in HBSS 0.2% glucose solution) for 5 minutes at 37 °C. Then mechanically in (0.05% DNase in growth medium: Neurobasal supplemented with B27, 1mM L-glutamine and penstrep) using a glass pasteur pipette until the solution is homogeneous. The solution is then strained with a 70 $\mu\text{m}$  cell strainer and added to FBS to centrifuge for 10 min at 1000RPM. The pellet was then mixed with growth medium, and cells were plated (40 000 cells per well) on Poly-D-lysine (100mg/ml- Gibco) pre-coated glass coverslips. Neurons were plated in the growth medium, and the medium was changed 2 hours after plating.

## 4 Results

### 4.1 NV defect results

The behaviour of the single NV defect was probed at 1D simulation without additional defects. Charge state dependency was probed as the function of laser power. In the simulation, charge state neutrality was respected. NV charge state at the simulation time  $t=0$  is in its neutral state,  $p(NV_0)=1$ .

### 4.1.1 Time simulation

Figure 14 shows the simulated time dependency of the charge state probability with the three different laser powers: 0.1mW, 1mW and 5mW. The first part of the trace shows an increasing population of the NV<sup>-</sup> charge state with elapsed time. A steady state is reached faster for the higher laser powers, and the population of the NV<sup>-</sup> charge state at equilibrium increases with the laser power as expected. Steady-state is reached after 5.6  $\mu$ s at the laser power of 0.1mW, after 190ns at 1mW, and after 78ns at 5mW with a charge state distribution (NV<sup>0</sup>/NV<sup>-</sup>) of  $\sim$ 31/69 % at 0.1mW,  $\sim$ 8/92 % at 1mW and  $\sim$ 2/98 % at a 5mW laser power. When the laser power excitation is increased to 5mW (Figure 14, blue trace), an inflection point in the NV<sup>-</sup> population can be seen at  $t = 6$ ns. This is due to the saturation of the excited state of NV<sup>-</sup> whose population is rising faster than the population of the metastable singlet state. After the occupancy of the metastable singlet state reaches its maximum, which is determined by its lifetime, a second saturation occurs. This is a consequence of the long-lived metastable singlet ground state with a lifetime of  $\sim$  200 ns at room temperature [44]. The visibility of the second inflexion point increases with the laser power, in accordance with [45].

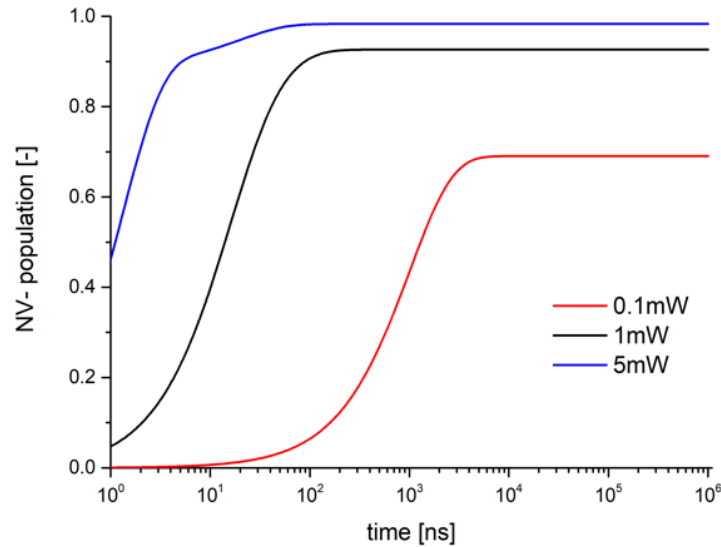


Figure 14 - The simulated time-dependent population of the NV<sup>-</sup> defect charge state without the presence of any other defects in the diamond crystal and without the resonant microwave field application. The system of partial differential equations was solved for three different laser powers (red – 0.1 mW, black – 1 mW, blue – 5 mW).

### 4.1.2 Laser power-dependent simulation

Figure 15A shows the simulated charge state populations of the NV<sup>-</sup> defect and of the metastable singlet state at steady state as a function of the laser power, with a resonant microwave field on or off. These traces are used for the calculation of the spin contrast in Figure 15B. The population of the NV<sup>-</sup> charge state starts to saturate at 1mW and is followed by saturation of the metastable singlet state at 1.5 mW. The population of NV<sup>-</sup> reaches a value of approximately 0.92. Results of the model show that saturation of the population of the NV<sup>-</sup> charge state is linked with the saturation of the metastable

singlet state, where most of the charge is stored. This is also in accordance with ref [35], where it is shown that at high laser powers, the charge is stored at the metastable singlet state. Figure 15B shows the optically/photoelectrically read spin-contrast of the single NV defect. Spin contrast has a maximum of 0.35mW of laser power with a value of 30%.

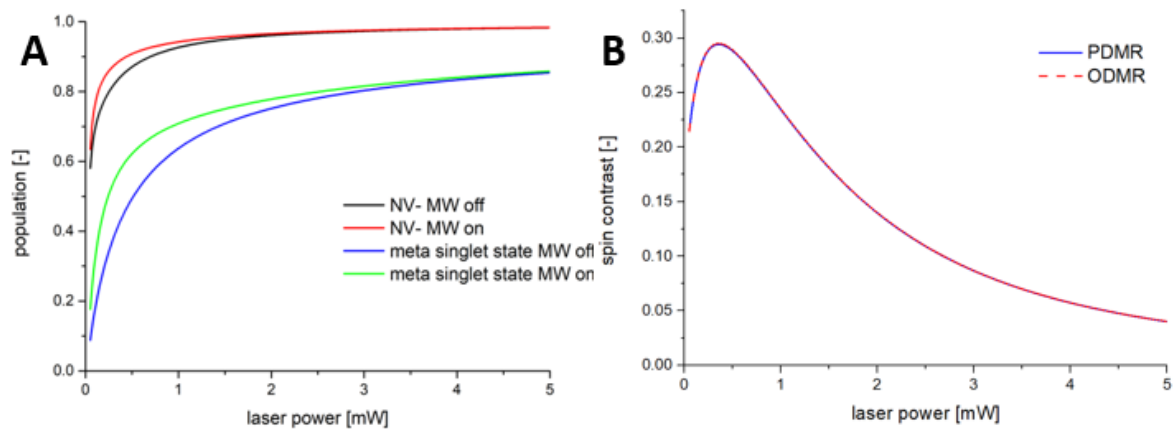


Figure 15 – A: The simulated laser power dependence of the population of the NV<sup>-</sup> charge state and the metastable state singlet at the steady state. The population of the NV<sup>-</sup> charge state is calculated with and without the resonant microwave field in black (MW off) and red colour (MW on), while the metastable singlet state population is represented in green (MW on) and blue colour (MW off). B: Laser power dependency of the spin-contrast at the single NV defect, ODMR (red trace, dashed line) and PDMR contrast (blue trace, solid)

### 4.1.3 Relaxation rates discussion

Two different sets (Wirtitsch - [35], Tetienne - [46]) of rates of relaxation from the metastable state singlet to the ground state ( $m_s=0$ ) are still under discussion. The simulation was performed with the locked ionisation rates (taken from the fitting of experimental data). Only results for the ODMR spin-contrast are shown since the PDMR is strongly affected by the presence of other optoelectrically active defects (chapter 4.2). The two modelled cases (Wirtitsch and Tetienne) differ slightly in the position of the maximal contrast in the PL intensity, and contrast decreases faster in the case of Tetienne's rate set due to the faster dropping of the initialisation efficiency. In particular, when using the data from Wirtitsch, the ODMR maximum contrast shifts slightly towards the higher laser power.

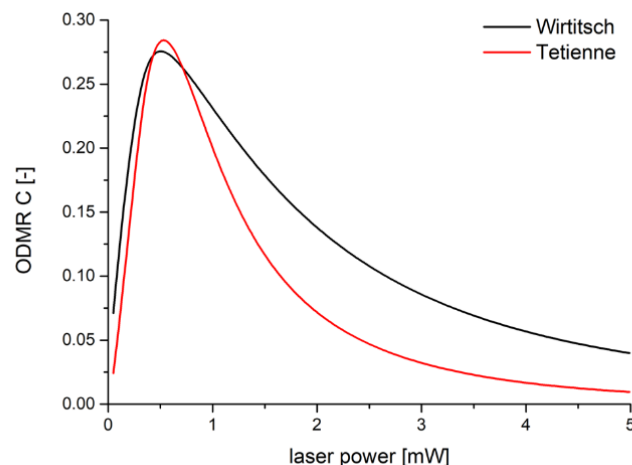


Figure 16 - Simulated laser power dependence of the CW-ODMR spin contrast in case of single NV and defect in the steady state. The figure shows ODMR contrast with the usage of Wirtitsch rates (black trace) and Tetienne rates (red trace).

## Conclusion and author contribution

Photodynamics of the single NV defect occupation for each energy level in time, and spin-contrast with laser power dependency were modelled. Computer simulation shows that for high large laser powers, the probability of NV<sup>-</sup> exceeds the probability of NV<sup>0</sup>, and most of the charge is stored at the metastable state singlet. This is confirming the results in reference [35]. We have shown that without the influence of recombination by other defects, PDMR contrast copies the ODMR contrast.

The author designed a comprehensive model of the photodynamics of the NV centre level occupation. The model integrates the interaction between laser and microwaves with defects alongside the transport of charge carriers crucial for modelling of photocurrent signals. Various simulations were conducted by the author to investigate relaxation rates from the metastable singlet and discusses disparities observed in the optical spin-contrast dependence on laser power.

## 4.2 Influence of environment on spin contrast

We probed the influence of several other optoelectrical active defects in the diamond crystal lattice, the substitutional nitrogen (N<sub>s</sub>) and acceptor level X (vacancies, di-vacancies, etc.), on the spin contrast. We consider the charge states N<sub>s</sub><sup>0</sup> and N<sub>s</sub><sup>+</sup> in our calculations [47, 48]. We assume that in the initial state, there is an equal probability for N<sub>s</sub> to be in the N<sub>s</sub><sup>0</sup> and N<sub>s</sub><sup>+</sup> charge states [47, 48], i.e. p(N<sub>s</sub><sup>0</sup>) = 0.5. In the same way, we are considering the charge and initial states of level X. The charge state neutrality was compensated by adding a hole with a probability of 0.5 inside the valence band.

### 4.2.1 Effect of N<sub>s</sub> centre

We simulated photodynamic of one NV and one N<sub>s</sub> centre. The total spin contrast is influenced by photoionisation from the N<sub>s</sub> level [45]. With our model, we can monitor the changes due to photoionisation and recombination of the charge carriers on individual defect levels. Figure 17A shows the laser power dependence of the occupation change in the total NV<sup>0</sup>, NV<sup>-</sup> excited state and N<sub>s</sub> populations when the MW excitation is changed from “on” to “off”.

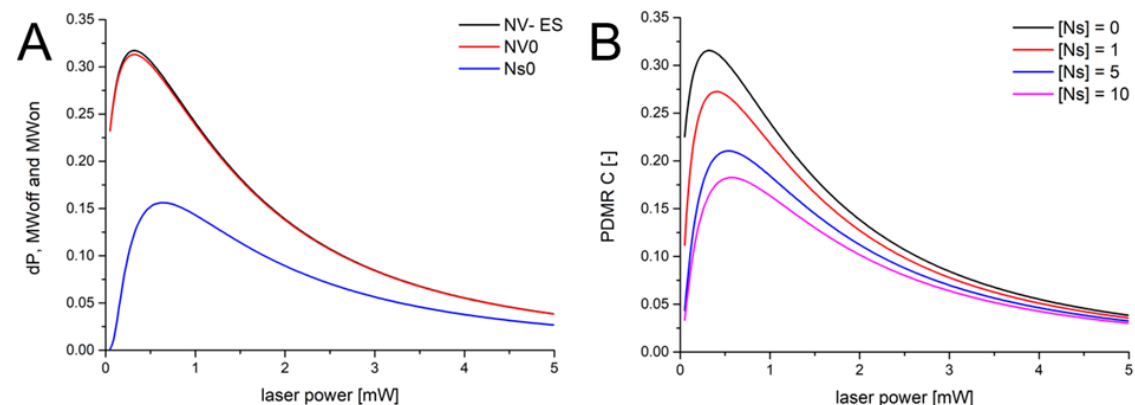


Figure 17 - A shows modelling of the occupation changes ( $dP$ ) of  $NV^-$  excited state,  $NV^0$  and  $N_S$  when the resonant microwave field is turned on and off when 1  $N_S^0$  centre and 1 NV centre under a 10 G microwave excitation is considered. B shows the laser power dependence of the total PDMR spin contrast for different numbers of  $N_S$  present. The total photocurrent (resulting from NV and  $N_S$  centres ionisation) is considered here. Traces of different colours represent the output of the model for 1 NV centre and various numbers of  $N_S$  centres, ranging from 0 (reference) to 10 (fraction  $N_S/NV$  of 10/1).

The calculation is done for a situation of 1  $N_S$  centre and 1 NV centre. Occupation change of the  $NV^-$  excited state coincides with the ODMR contrast as well as with the PDMR contrast for the case of 0  $N_S$ . That is because the photoluminescence is proportional to the excited state population, as is the photocurrent in the absence of  $N_S$ . Notably,  $N_S^0$  occupation is influenced by the microwave field. This is to be expected as  $NV^0$  occupation drops, which leads to the creation of a hole in the valence band. Also, the  $NV^0$  occupation change is practically identical to the  $NV^-$  occupation change, meaning that the changes in the  $m_S = 0/\pm 1$  can also be potentially monitored by the  $NV^0$  population changes, or with less contrast even by  $N_S^0$  population change, which brings interesting alternatives for the PDMR detection and spin readout applications.

Figure 17B depicts the predicted spin contrast on the total photocurrent as a function of the number of  $N_S$  centres placed in the central bin together with an NV centre. A significant decrease and a shift of the maximum in the electron spin contrast to higher powers is observed when the number of  $N_S$  defects introduced to the system increases, as already documented experimentally [45]. As a direct use of the modelling, from the detected shift in the maximum of the PDMR contrast as a function of the laser power, we are able to evaluate how many  $N_S$  centres are present in the close vicinity of the NV centre. As the  $N_S$  presence also has consequences on the reduction of the  $T_2$  and  $T_2^*$  times, our model can be useful for evaluating the number of  $N_S$  centres in the close vicinity of NV, helping thus devising the origin of the spin decoherence in single NV centres.

We apply the model to the experimentally measured dependence of the optically and photoelectrically detected spin contrasts of a single NV centre. Considering the 20ppb nitrogen concentration and the focus point volume of roughly  $1\mu m^3$ , we estimate the number of  $N_S$  that have an impact on PDMR contrast to be around 10. All of the rates, except for ionisation and recombination, were taken from the literature (see Appendix A for details). Concerning the rates  $k_5$  and  $k_6$ , there is no consensus at this point on these rates, therefore we apply the model twice – first, we consider the rates from Wirtitsch et al.[35], then the rates from Tetienne et al.[46], and get the ionisation and recombination rates for both cases (Figure 18C).

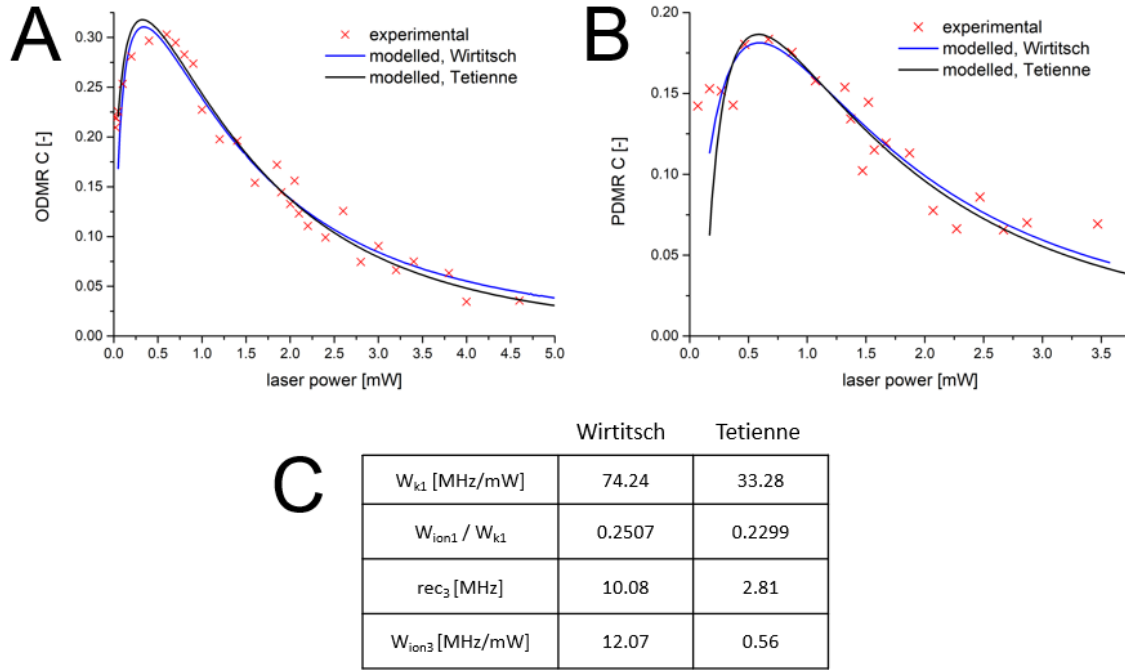


Figure 18 - Laser power dependence of the ODMR/PDMR spin contrast for a diamond quantum chip. A: shows experimental (red crosses), modelled with Wirtitsch rates [35] (blue trace) and with Tetienne [46] rates (black trace) photoluminescence contrast. B: shows experimental (red crosses), modelled with Wirtitsch rates [35] (blue trace) and with Tetienne rates [46] (black trace) photocurrent contrast leading to an estimated  $N_s$  concentration of  $10 N_s$  for 1 measured NV. For this reason, we used the same  $N_s$  concentration for ODMR modelling. C: contains values of the FIT for the rate set of Tetienne [46] and Wirtitsch [35] and shows the result of the model in the form of ionisation and recombination rates for the two different sets of input rates (mainly differing in  $k_5$  and  $k_6$ ).

Figure 18 shows a comparison of experimental contrast (red crosses) with the output of the modelled system (blue trace) for both ODMR (Figure 18A) and PDMR (Figure 18B). Figure 18A shows that the ODMR contrast peaks at approximately 30 % at about 0.4 mW laser power. Figure 18B shows the experimental and modelled PDMR contrast reduced by  $N_s$  defects, where the maximum is approximately 18 % under 1.2 mW laser power (blue trace). Figure 18B also shows a clear significant shift of PDMR contrast maximum that is believed to be caused by the effect of the  $N_s$  defect, as shown by modelling.

The ODMR modelling trace for Figure 18A is then recalculated for an identical number of  $N_s$  centres. From the modelling, we can conclude that, as expected, the ODMR spin contrast is not significantly influenced by the  $N_s$  presence, while the PDMR contrast is. From the output of the model (Figure 18), we can see that the recombination rate “ $rec_3$ ” is significantly closer to the previously reported value of  $3n_s$  [49] for the case of the input rates from Wirtitsch et al.

Notably, by using our theoretical model for the measured ODMR and PDMR spin contrast, we can also calculate the quantum efficiency (QE) for both optical and photoelectric detections.

Figure 19 shows the laser power dependence of the fluorescence and photocurrent QE. In the low laser power regime, we can see a maximum optical QE of 84% in the presence of MW and 69% without MW. The optical QE decreases with the laser power. As concerns PDMR, above 2.2mW, the photocurrent QE increases with the laser power and starts to dominate the optical QE, reaching ~ 44%

at 4mW; however, at this laser power, the photoelectrical spin contrast drops to 10% (Figure 17B). The results of our model are in good agreement with the experimental data of QE. In particular, the PL quantum efficiency calculated using our model is very close to the results presented in reference [50], where the PL QE of the NV centre was measured. In addition to this work, our modelling enables us to obtain the QE for the case of photoionisation. Modelling shows that for higher laser powers, the charge carrier generation becomes more effective than the photon generation by photoluminescence. Despite the decrease in spin contrast, the total photocurrent signal increases with the laser power without saturation, which can be effectively used to reach a higher sensitivity for spin magnetometry. Interestingly, as the photocurrent and PL are complementary, one could extend this measurement concept to measure electron and photon count correlations, which we plan in the future. Further on, we can see from Figure 19 that the experimental photocurrent QE that is calculated from total collected photocurrent is lower than the theoretical QE trace for 1 NV without  $N_s$  defect that is calculated from the generation of charge carriers. The decrease in the QE is caused by the fact that the lifetime of the charge carriers is shorter due to the presence of the other defects ( $N_s$ ). On the contrary, if we do the modelling for 10  $N_s$ , the modelling matches the experiment well.

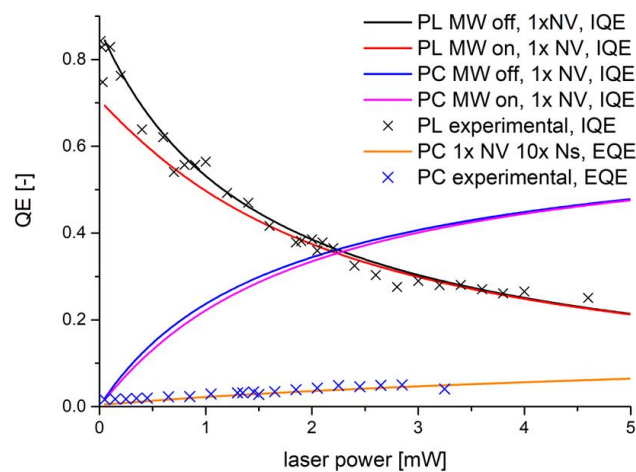


Figure 19 - Laser power dependence of quantum efficiency. The figure shows the quantum efficiency model of the photoluminescence without (black trace) and with (red trace) microwave excitation for single NV and experimental PL data (black crosses) and the model photocurrent quantum efficiency without (blue trace) and with (pink trace) microwave excitation for 1 NV. The traces are calculated from the PL and photocurrent dependence as a function of the laser power. For the PL data, we scaled the experimental data onto the theoretical curve to compare the experimental trace shape with the model. The orange trace is the modelled photocurrent quantum efficiency for the case of 1 NV and 10  $N_s$ , and blue crosses correspond to the experimental photocurrent data. The experimental photocurrent data are fitted directly without any scaling.

#### 4.2.2 Effect of acceptor level (level X)

For the study of the acceptor defect, we consider the density of  $N_s/NV$  as 11/1, and we vary the density of the acceptor level  $[X]=0$  to  $[X]=7$ . Calculations performed using this model before show that when only NV and  $N_s^0$  are present, the magnetic resonances formed in the photocurrent are always negative, regardless of the green laser power applied or of the value considered for the different recombination rates. The formation of positive resonances phenomena requires the introduction of an acceptor level

and to consider that the positively charged state of this defect ( $X^+$ ) presents a large electron capture cross-section (considered 20 times higher than the electron capture cross-section of  $N_5^+$  to obtain the data presented in Figure 20). It can be observed in Figure 20A that the introduction of a small amount (1 to 4) of acceptor defect X in the model leads to an increase in the absolute value of the negative PDMR contrast. If a sufficient number of defect X is introduced into the mathematical model ( $[X] \geq 6$  in Figure 20A), the calculated green-light power dependence of the PDMR contrast appears qualitatively similar to the experimentally observed.

In the case  $[X]=6$ , calculations of the microwave-induced spin contrast (Figure 20B) indicate that the photocurrent resulting from  $NV^-$  and  $NV^0$  ionization decreases at resonance (negative contrast up to -20%).  $N_5^0$ -associated photocurrent also presents a large negative contrast (up to -22%), resulting, as explained above, from charge exchanges between  $NV^-$  and  $N_5^+$ . The microwave-induced contrast in the electron photocurrent (resulting from  $NV^-$  and  $N_5^0$  ionisation) is, therefore, always negative. On the contrary, under low illumination, the photocurrent associated with  $X^+$  ionisation increases at resonance, as expected, considering the capture of free electrons resulting from  $NV^-$  ionization by this defect. In case the concentration of defect X with respect to NV and  $N_5$  is sufficient, this causes an augmentation of the hole photocurrent at resonance and ultimately leads to the positive contrast observed in the total photocurrent under low-power green illumination.

These simulations clearly suggest that in the presence of acceptor defects, the hole photocurrent limits the PDMR contrast and, in some particular conditions, can lead to an inversion in the sign of PDMR resonances.

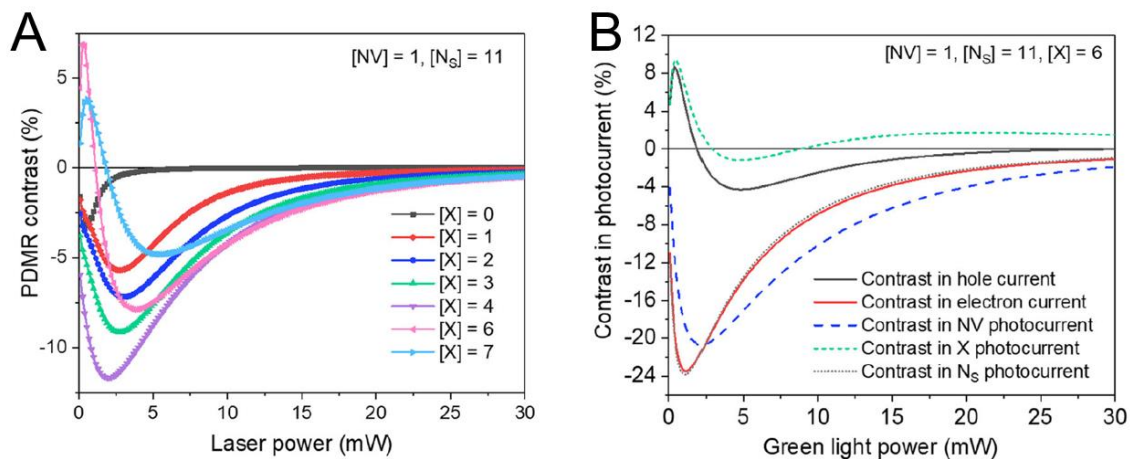


Figure 20 – A: Calculated green-light power dependence of the PDMR contrast for the different numbers of acceptor defects X. [X]: number of defect X, considering 1 NV center and 11  $N_5$  defects. B: In the case  $[X]=6$ , the MW-induced contrast in the total hole photocurrent and the total electron photocurrent was calculated, as well as in the photocurrent associated with  $N_5$ , X, and NV ionisation.

## Conclusion and author contribution

The author investigated the impact of the crystal defect environment on photocurrent generated from the NV defect by modelling. This involved influence of substitutional  $N_5$  and an additional acceptor level X and varying the density of the  $N_5$  defect and analysing the response of the PDMR contrast.

Observations reveal a decrease in PDMR contrast and a shift of its maximum to higher laser power with increasing  $N_s$  density. The model was validated by fitting experimental data from a single NV with the modelled contrast for both spin contrast (ODMR and PDMR). Alternations in model outputs were further discussed using different rates (proposed by Wirtitsch and Tetienne [35, 46]). Quantum efficiency (QE) modelling was conducted for the single NV defect, which was consistent with prior research, as well as for NV and  $N_s$  defect systems. Comparison of experimentally and theoretically obtained QE values demonstrated good agreement. The author developed the modelling of a new acceptor level X that accounts for the recently discovered positive resonances in the spectra of PDMR, particularly IIa crystals (Author worked on relevant publication {1}).

The author conducted simulations to assess the combined impact of various densities of other defects ( $N_s$ , X) on the photocurrent signal. Absolute values for NV ionisation, as well as other defects, were derived by fitting of experimental data. Furthermore, the author quantified the optical and photoelectrical quantum efficiencies of an individual NV centre, as well as the photoelectrical quantum efficiency of the NV complex within the crystal environment. Measurements of single NV were made by a PhD student, Michael Petrov (UHasselt, Quantum Science and Technology), and measurements of positive PDMR were performed by an experienced senior researcher, Emillie Bourgeois (UHasselt, Quantum Science and Technology).

### 4.2.3 GSLAC-assisted electrical readout

Microwave free detection of magnetic fields is a novel way for magnetometer sensor, utilising the GSLAC, developed in the thesis. Investigation of the magnetic resonance that originated from the ground state level anti-crossing (GSLAC) was performed for both types of read-out (optical as well as photoelectrical) and using irradiated the HPHT diamonds. On the surface of the diamond ohmic Ti/Al coplanar electrodes with a  $5\mu\text{m}$  gap were fabricated by standard lithography process. To compare the experiment with the model, we calculated PC and PL signals from experimental and geometrical conditions and reproduced them using the proposed model Figure 21A and Figure 21B show the predicted and measured laser power dependency at the total PL and PC signal. It can be seen that the photocurrent signal did not reach saturation, which is consistent with the previously published models. The photoluminescence signal should saturate due to the limit established by the  $\text{NV}^-$  excited state lifetime and be stacked into the metastable state singlet. The deviation in the PL model output and experiment can be accounted for by the shadowing of the diamond by electrodes, resulting in the reduction of the effective laser power. Figure 21C shows the total PC and PL signal as the function of depth (z axe) below the crystal surface. The local contribution is indicated by a blue (PC) or red (PL) shaded area (in arbitrary units). Results show that 90% of the PC signal comes from the region 0-30 $\mu\text{m}$  below the surface where the NV defects experience sufficient both optical excitation and electric field to drive the charge carriers towards the electrodes. PL signal is produced throughout the diamond slap and detected once photons get out of the high E-field region beneath the electrodes. Based on the simulation, we estimate the ratio of effective interrogation volumes of PC to PL detection to be the order of 1:20.

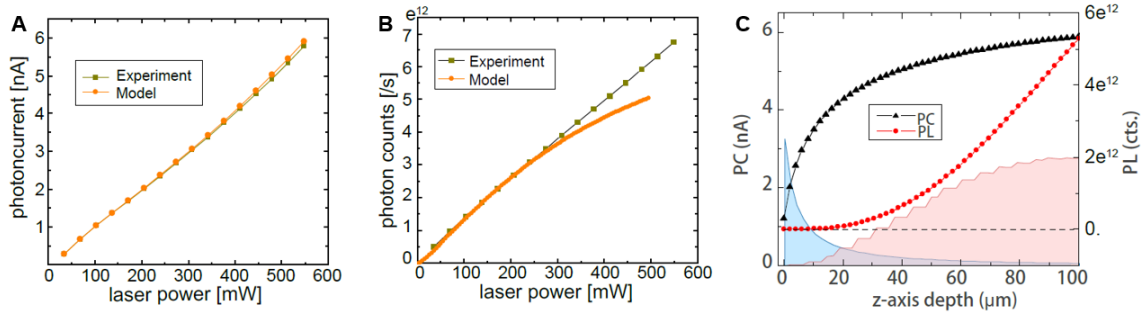


Figure 21 - A: calculated (orange) and experimental (green) total photocurrent vs laser power. B: calculated (orange) and experimental (green) photoluminescence signal vs laser power. C: calculated accumulated photocurrent (black) and photoluminescence (red) signal as a function of penetrating depth into the diamond chip. Blue (red) shaded area indicates local contribution to the photocurrent (photoluminescence) signal in arbitrary units.

## Conclusion and author contribution

A microwave-free diamond quantum sensor based on GSLAC-assisted photoelectrical readout for measuring weak magnetic fields was developed in this work in collaboration with the scientific group at Mainz University. Generation of both types of signals (photoluminescence as well as photocurrent) was quantitatively modelled in this thesis and relevant publication. (Author work in relevant publication {2}). GSLAC features were observed for the first time by photoelectrical readout. Information obtained from this work can be used to build hybrid gradiometers, taking advantage of observed detection volumes of PC and PL signals and improving spatial resolution.

The author determined the dependence of photoelectrical and fluorescence signals with crystal depth using his model developed in the thesis. The author also calculated the cumulative signal as a function of laser power. Measurements were performed by Huijie Zheng et al. at Mainz University.

## 4.3 Chip testing

Numerical modelling on both proposed chips in frequency ranges from 2GHz to 4GHz for 1W microwave power input was performed.

### 4.3.1 Chip for single crystal diamond

The initial phase of the testing was focused on modelling the chip's capability to deliver adequate microwave excitation. Figure 22 shows the result of the magnetic part of the microwave that is responsible for spin-flip from ground state  $m_s=0$  to  $m_s=\pm 1$ . Red arrows in the figure denote the orientation of the field (determined by  $H_x$  and  $H_y$ ), with their lengths proportional to the field intensity. Figure 22A shows a comprehensive view of the chip from the YZ plane. Results show that the highest field intensity occurs around the edges of the microstrip, diminishing towards the upper surface of the diamond (highlighted by the red square). The region of interest for sensing lies beneath the laser aperture, roughly spanning from the diamond's upper surface to  $100\mu\text{m}$  below it (indicated by a yellow ellipse). In this region, the generation of fluorescence and photocurrent signals from NV centers

predominate. Figure 22B shows the magnified area pertinent for sensing. The diamond crystal is highlighted by the red square, while the laser aperture is marked by a green square. Results show that beneath the laser aperture, the microstrip established a homogeneous field with a strength of  $\sim 40\text{A/m}$ . The disparity in field intensity between the crystal surface and  $100\mu\text{m}$  below is approximately 10%. The direction of the field indicates that NV defects aligned with their axes parallel to the Z-axis of the model experience maximal microwave stimulation.

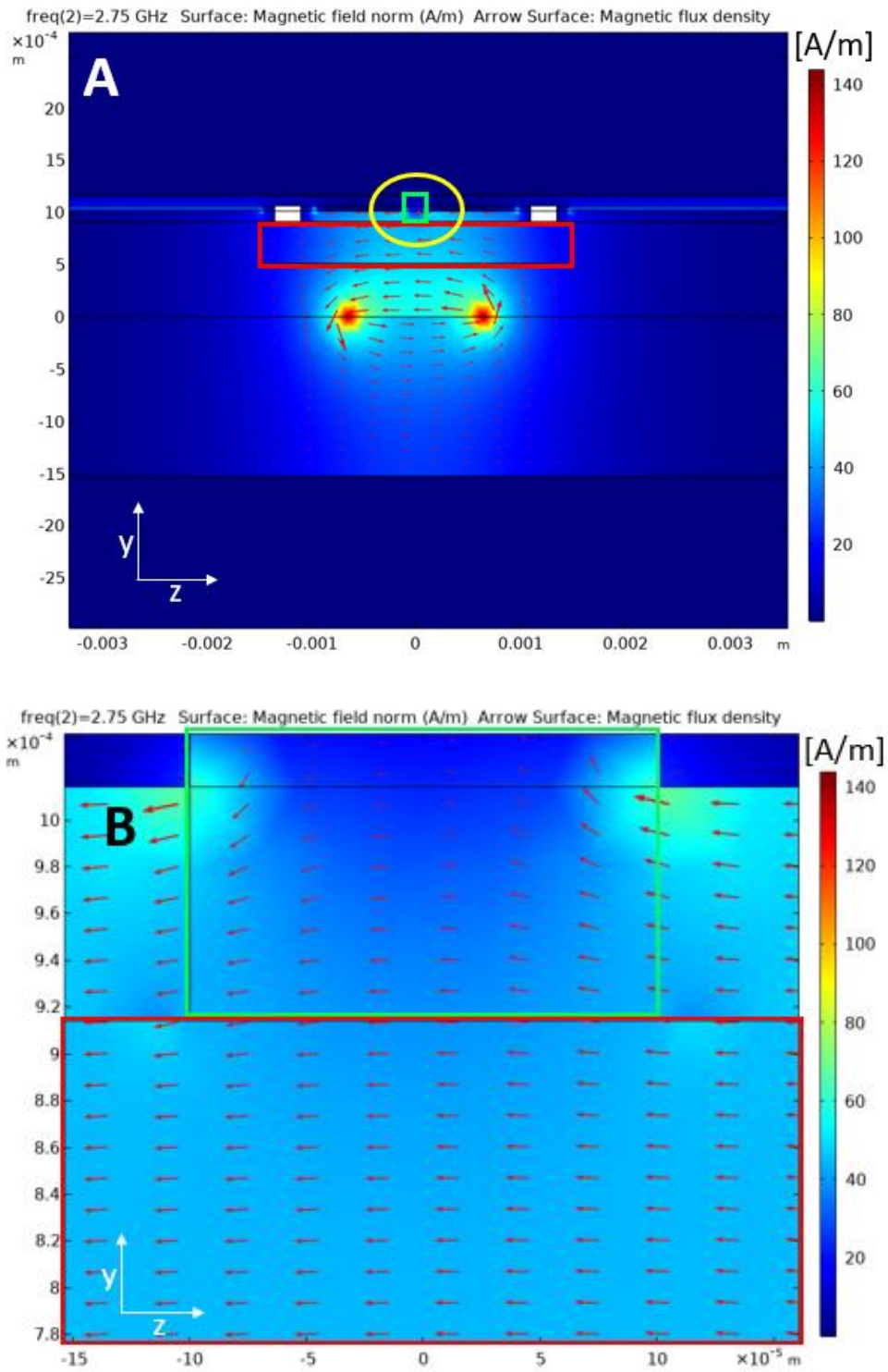


Figure 22 – Microwave field distribution (H part) in YZ plane. The green box stays for the laser aperture, red box for the single crystal diamond sample. A: Total microwave H field distribution in chip in A/m for the frequency of 2.75GHz, yellow circle stays for the magnified area depicted at B. B: the magnified area around the laser aperture. V3 stays for layer 3 and V4 for layer 4.

Figure 23A shows the computed S-parameters delivered from the numerical model, where  $|S_{11}|$  denotes the microwave power reflected to the source port, and  $|S_{21}|$  stands for the transmitted power to the terminator. The results exhibit an anticipated profile in both  $|S_{11}|$  and  $|S_{21}|$  parameters, consistent with microstrip behaviour. Notably, minimal microwave power is transmitted to the electrode lines, which is a crucial aspect for detecting small photocurrents, such as those generated by a single NV. Figure 23B shows the experimental data demonstrating the microwave-induced variation in the photocurrent for the three different chip types. Results indicate that the proposed chip design exhibits minimal fluctuation in photocurrent intensity compared to conventional ‘parallel’ (main text Figure 49B) and ‘perpendicular’ (main text Figure 49B) chips commonly used by the UHasselt group. All of the experiments were performed at the same diamond crystal and electrodes (described in chapter 3.3.1). Microwave excitation in the case of ‘parallel’ and ‘perpendicular’ chips was made by the wire that lay at the microwave surface (depicted in chapter 2.2 and Figure 4). Flat frequency response in photocurrent is crucial for accurately measuring low-intensity photocurrent, particularly photocurrent from the single NV defect.

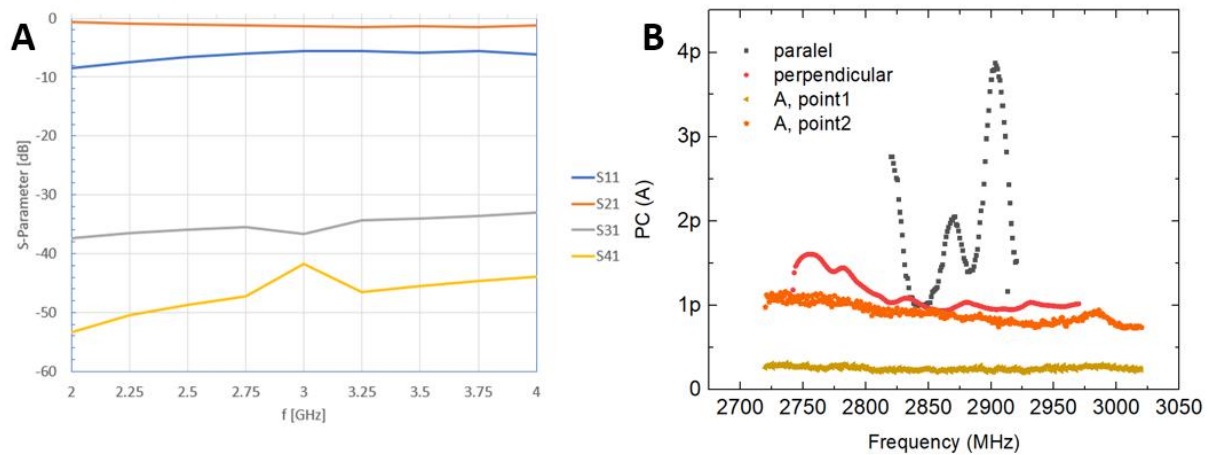


Figure 23 – A: S parameters of the chip for the single crystal diamond. S11 stands for the power reflected back to the microwave source, S21 stands for the microwave power transmitted to the terminator, and S31 and S41 stay for the microwave transmitted to the electrode lines. B: Microwave involved pickup response to the DC photocurrent. Parallel stands for the chip with parallel lines (measured with lock-in), perpendicular stands for the chip with perpendicular lines (measured with lock-in), A stays for the proposed chip, point1 and point2 are two different focus points at the diamond crystal.

## Chip for single crystal diamond, pulse measurements

We performed multiple series of ODMR pulse sequences, including Rabi, Ramsay, and Hans echo, on the designed chip to assess its functionality for microfluidic applications for measuring NMR. While comprehensive usage of this chip for NMR is currently underway, here we present the Rabi sequence. To demonstrate coherent control of quantum states ( $m_s = 0$  and  $m_s = \pm 1$ ), we perform the Rabi protocol, which starts with a laser polarization pulse to put the electron spin population into the  $m_s = 0$  state. The polarization pulse typically takes 3-5 $\mu$ s. A MW pulse with a width of  $\tau_{MW}$ , follows a polarization pulse to drive transition between the ground and excited states. Immediately after, a 2 $\mu$ s laser readout pulse is applied to measure the state of the electron spin. This represents a typical Rabi protocol without lock-in detection. To suppress the effect of the low-frequency noise sources in our measurement, we have implemented a lock-in detection technique. To implement lock-in detection,

we periodically modulate the amplitude of the MW with a frequency typically of 20 kHz. To reveal Rabi oscillations, we varied  $\tau_{MW}$  and monitor the in-phase signal of Lock-in (Figure 24).

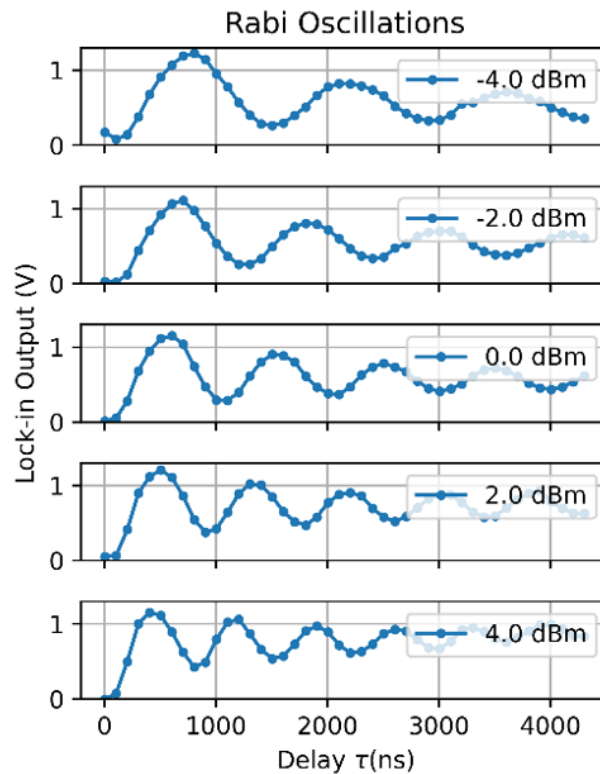


Figure 24 - Rabi oscillation performed at QNMR chip for the five different microwave powers. Amplitudes represent the output of the MW source before being amplified by a MW amplifier with a nominal gain of 45 dB.

### 4.3.2 Chip for NDs

The geometric of the omega-shape structure was varied to investigate their influence on the resonance profile, particularly in terms of the  $|S_{11}|$  (denotes microwave power reflected to the source port (reflection coefficient)) parameter, in proximity to the 2.87GHz frequency. Alternations were made on both the inner diameter of the omega and the diameter of the aperture to discern their impact on the resonance characteristics. Figure 25 shows the frequency dependence of the  $|S_{11}|$  parameter for the different inner diameter of the omega structure. Results show that optimal diameter for the omega is 4.5mm. This fulfils the criteria for potential resonance patterns, and also provides ample space for neuron cultivation.

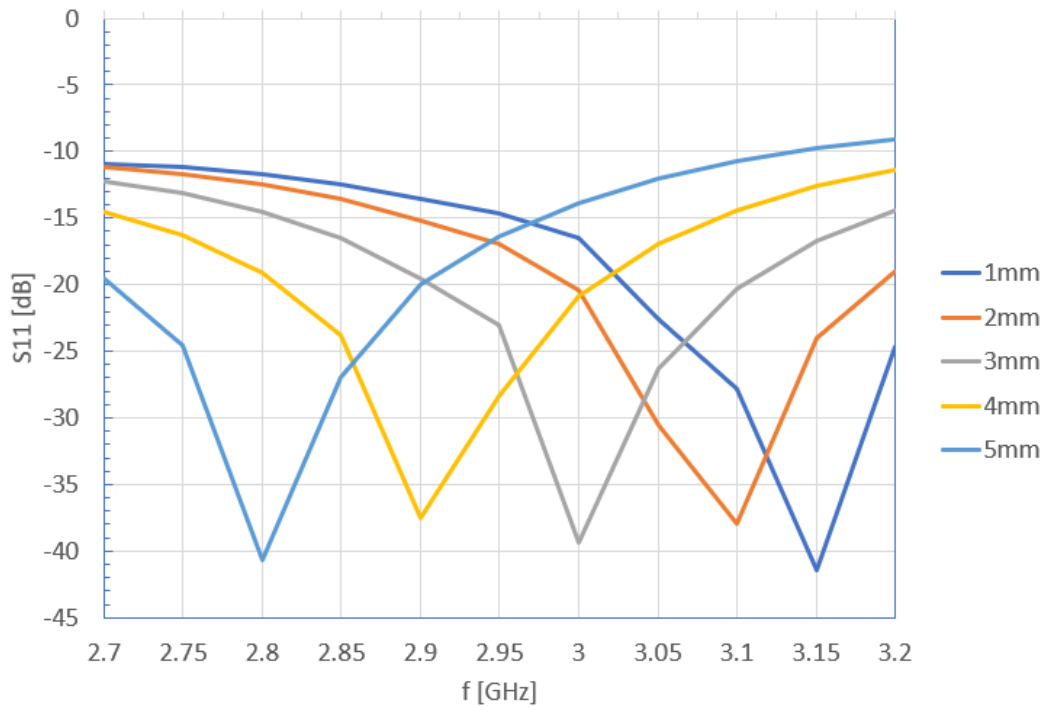


Figure 25 – Frequency dependence of the  $|S_{11}|$  parameter on the inner diameter of the omega. Values at mm represent the corresponding value of the omega diameter.

The performance of omega-shaped antenna in terms of its ability to regulate the temperature regulation through off-resonance MW absorption in the liquid was evaluated by modelling. To characterise the performance, a single microwave fluorescence sweep was conducted at two different temperatures with 1mW of laser excitation. Normalised fluorescence is presented in Figure 26A. Spectra show temperature-induced shifts alongside Zero Field Split with an observed spin contrast (ODMR) of approximately 3%. Using the local minimum algorithm (employing the key MatLab function 'islocalmin'), we accurately determined the peak positions (+1 and -1 energy levels of ground state  $NV^{\cdot-}$ ) in each spectrum. The peak detection enables real-time monitoring of the temperature within the imaging medium, determining the assessment of microwave-induced heating and its correlation with the temperature stabilisation capabilities of the omega-shaped structure. Results of microwave-induced temperature maintenance of the imaging media can be seen in Figure 26B. The blue curve shows the temperature prediction by the model, and the orange curve represents experimental data measured via the nanodiamonds. Both spectra show similar trends, with a sharp rise in temperature within 5 minutes followed by a slow rise towards a steady state of 40°C. For the simulation, we used a microwave power of 5W. For the experiment, we used a microwave power of 10W and a laser power of 1mW of laser power, whilst microwave frequency was 2.87GHz. The difference between microwave power used in simulation and in measurements is caused by power loss in MW cables and connections as well as the discrepancy between the material and environmental temperature.

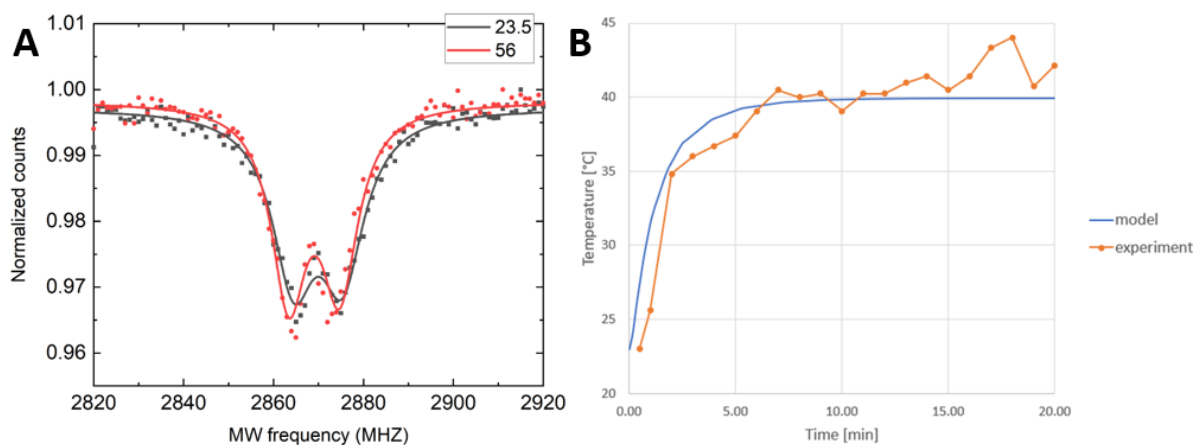


Figure 26 – A: Normalised intensity of fluorescence emission from NDs using the omega shape chip. Data represent two different media temperatures, 23.5 and 56 °C. Two peaks correspond to the split of energy level (+1 and -1) of NV- ground state due to Zero Field Split (ZFS). Spectra were taken with 1mW of laser excitation by a green 532nm laser and 1W microwave power. B: Microwave (2.87GHz) induced temperature of the liquid sample modelled (blue) and sensed by NDs (orange) with the usage of an omega-shaped antenna. For the excitation, 1mW laser power (532nm) and 10W microwave power were used, and for the modelling, 5W of microwave power was used.

Figure 27A shows the photoluminescence map of neurons with attached nanodiamonds (red ellipse). Figure 27B shows ODMR spectra for the attached nanodiamond from the ND particle marked by green ellipse in Figure 27A. Spectra was taken at a laser power of 1mW and 2W microwave power. ODMR spectra show Zero Field Splitting. Figure 27A also shows the successful anchoring of functionalised nanodiamond particles on the extracellular part of the cell membrane. Nanodiamonds were equipped with a poly(glycerol) coating and modified with a ligand which selectively and tightly binds to the CXCR4 receptor. CXCR4 is a non-internalizing receptor enabling a long-term anchoring of the nanodiamonds on the membrane. The biocompatibility of the modified NDs is evidenced by the sustained fluorescence signal emitted by the particles throughout the neuron’s one-hour lifespan within the chip. These observations are consistently reproducible across multiple measurements. The stable attachment of NDs on the neural membrane is an important research question and neuron receptor targeting was demonstrated in the work carried out here. It should be mentioned that the CXCR4 has been linked at the Institute for Organics Chemistry and Biochemistry.

Our results demonstrate the efficacy of nanodiamonds as a biocompatible tool for in vitro quantum sensing of both magnetic and temperature fields. The chip functionality corresponding well the design predicted by the COMSOL simulations.

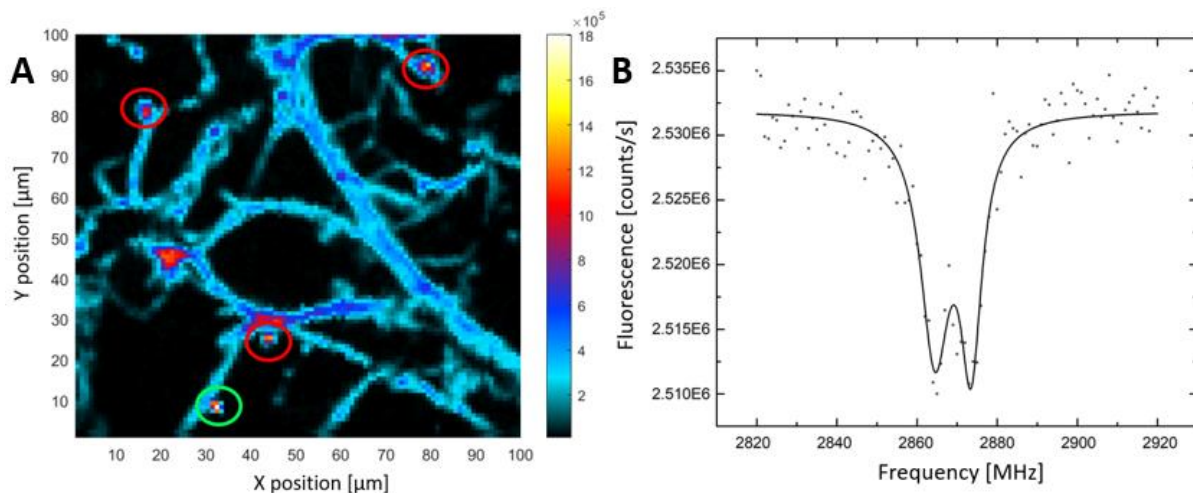


Figure 27 – A: Photoluminescence map of the neuron with attached nanodiamonds (in red ellipses), green ellipse marks the ND from where spectra were taken. For excitation, a 532nm laser with 1mW power was used. B: ODMR spectra taken from the nanodiamond attached to the neuron. Spectra was taken at lab temperature with 1mW of laser and 1W of microwave power.

## Conclusion and author contribution

Both types of quantum chips, designed for use with single-crystal diamond and nanodiamond particles, were subjected to both theoretical and experimental scrutiny. Theoretical testing was conducted through numerical modelling, focusing on microwave-related characteristics such as S parameters and field distribution. Additionally, the single crystal diamond chip was tested for microwave pickup theoretically by examining  $|S_{31}|$  and  $|S_{41}|$  parameters (microwave transmitted to the electrode lines). Experimentally, we designed and conducted measurements of the microwave-induced pickup, where the proposed chip exhibits improved performance compared to currently employed chips. We verified the device functionality by performing series of pulse sequences, including Rabi, Ramsay, and Hahn echo, on a chip modification used for microfluidic QNMR. Results show that the chip gives good spin manipulation possibilities and suits for microfluidic manufacturing. The Omega-shaped chip underwent examination of its heating properties alongside measurements conducted on ND particles heating. Numerical modelling was employed to analyse heating characteristics, while microwave heating of liquid media, sensed by NDs, was experimentally determined. Optical detection of Zeeman splitting was conducted using liquid imaging, which is considered representative of biological samples, as well as nanodiamonds attached to neurons. Our finding substantiates the viability of utilising ND quantum probes to measure physical fields, including temperature and magnetic fields, for *in vitro* applications.

The author tested both models theoretically and iterated the chip design using numerical model output. Measurements were carried at the UHasselt, Quantum Science & Technology Group in collaboration with UHasselt BIOMED. Neurons were cultivated by PhD student Sarra Zaghbouni. Measurements on the Omega antenna were performed by a PhD student, Alevtina Shmakova, measurements on the single crystal chip were performed by a PhD student, Michal Petrov, and the QNMR variation chip was experimentally tested by senior expert researcher Reza Tavakoli. Nanodiamonds particles were functionalised by Synthetic Nanochemistry Group in Prague.

## 5 Conclusion

This thesis's main aim was to study quantum chips for sensing the environmental interactions with a future use in biological systems utilizing the nitrogen-vacancy (NV) point defect within the diamond's crystal lattice. The NV defect exhibits energy level shifts in response to external electromagnetic fields, which can be readout in optically or photoelectrically. For understanding of the relationship between the output signal, microwave/laser excitation and crystal environment, a sophisticated model was developed, containing the intrinsic behaviour of the NV defect, its interaction with laser and microwave fields, and its interplay with other defects, notably substitutional nitrogen (Ns). Understanding the physical processes behind signal generation is essential for the advancement of quantum sensors. Based on the described NV behaviours, two types of quantum chips were designed and fabricated: one for single crystal diamond application and the other for sensing within nanodiamonds (NDs). Both chips underwent rigorous numerical modelling and experimental verification. Furthermore, the chip designed for single crystal diamond exhibited promise for future application in microfluidic devices, while the ND-based quantum sensor was tested with particles affixed to the neuron bodies, showcasing its potential in biological sensing applications. All goals were fulfilled and are listed below:

### **Rate equation model of the NV defect in presence of the drift**

The author developed a full mathematical model describing the temporal dynamics of the occupation of the NV defect in the diamond lattice based on the differential rate equation for each energy level, taking into account laser and microwave interaction, charge carrier drift and recombination kinetics. This original model is essential for the enabling highly performing NV quantum chips based on photoelectric spin state readout.

### **Crystal environment modelling of NV center**

The author investigated the effect of the crystal defect environment on NV defects by incorporating additional defects (substitutional nitrogen and acceptor defects) into the nearby diamond lattice. Their influence on the photocurrent signal was examined. The author systematically characterised the dependency of the photocurrent signal on the density of these defects. To account for defect interactions, conduction and valence bands were introduced alongside the migration of charge carriers. The author modelled total quantum efficiency for both the single NV defect and the crystal environment containing NV and Ns. The developed model allows to estimate Ns concentration in the close vicinity of the NV centre, which has important effect on the spin dynamics and consequently on the spin contrast which is inherent part of the magnetic field and temperature sensor.

### **Experimental verification of the proposed models**

The author experimentally verified the proposed model through the measurements of fluorescence and photocurrent signals of individual NV centre. The author conducted data fitting to determine ionisation rate values, which are dependent on the optical system. It was shown that the simulated spin-contrast closely matched experimental data. The author also investigated the influence of the acceptor defect on the positive PDMR phenomena. Additionally, the author explored signal generation as a function of the depth beneath the crystal surface. The variation of the model confirmed its applicability on the control of the NV spin sensor, and it is important for setting up operational parameters of device for optimal detection performance.

### **Chip designing and manufacturing.**

Based on the physical understanding of NV behaviour, the author developed two quantum chips, the first for the single crystal diamond application and the second for nanodiamond applications. Each design was simulated for microwave field distribution and resonance patterns. The author developed electrodes specific to single crystal diamond, aimed at minimizing potential microwave crosstalk interference. Subsequently, prototypes were assembled by the author and primed for experimental interrogation. These prototypes are currently used for designing practical sensors. As future step we will use the developed methodology for measuring the temperature in TRPV channels using nanodiamond, which application brings an important hope for studying of neuropathologic diseases.

### **Chip testing on fantoms**

The author's quantum sensor for single-crystal diamond applications has been tested for microwave-coupled sensing. Additionally, a QNMR microfluidic variant was employed to evaluate basic qubit manipulation using pulse schemes. Furthermore, the heating capabilities of the omega-shaped sensor for ND particles were assessed in liquid media.

### **Chip testing on the biological environment**

The sensor developed for the ND application has been tested for magnetic field sensing in the real biological system, where NDs are attached *in vitro* to neuron axons. The concept of using NV as a sensor for quantum detection was shown.

## 5.1 NV defect model

The author modelled the NV defect at two possible charge states, NV<sup>-</sup> (five energy levels) and NV<sup>0</sup> (single energy level). Photodynamics were elucidated by a set of rate equations formulated to describe the transition between energy levels. Spin contrast was modelled for both types of readout methods, optical and photoelectrical. Notably, the steady-state probability distribution of the charge states as a function of laser power was characterised alongside the time dependency of the metastable state singlet. Results show that the majority of the charge state probability in the charging probability in the metastable singlet state causes an increase in the charge probability in the metastable singlet state, causing an increase in the charge probability in the NV<sup>-</sup> charge state at higher laser powers. Furthermore, analysis of laser-dependence spin-contrast shows that with the absence of the recombination centres, PDMR contrast copies that of ODMR one.

## 5.2 Influence of the environment on spin contrast

Two additional defect structures, namely substitutional nitrogen (Ns) and a proposed acceptor level X, were incorporated into the model, each considered as a single energy level structure with possible positive (Ns<sup>+</sup> X<sup>+</sup>) or neutral (Ns<sup>0</sup>, X<sup>0</sup>) states. Variation in the density of Ns centres was systematically

explored, elucidating its impact on the photocurrent readout of spin-contrast. Our analysis shows that an increase in  $N_s$  led to a reduction in the PDMR contrast, accompanied by a shift of its maximum to higher laser power, which is consistent with experimental observations. The validity of the model was further substantiated through spin-contrast measurements of individual NV centres employing both optical and photoelectrical readout, demonstrating excellent agreement with experimental data. Upon comprehensive model determination, we calculated quantum efficiency for both optical and photoelectrical readout, as well as for NV and  $N_s$  complexes. Introducing acceptor level X into the simulated crystal environment enabled modelling of non-standard phenomena such as positive PDMR. Computer simulations of level X density showed that the origin of the positive PDMR may come from the proposed acceptor level. Furthermore, we investigate the depth-dependent origin of the signal, revealing theoretically and experimentally that 90% of the photoelectrical signal comes from the region 0-30 $\mu\text{m}$  below the crystal surface, in contrast to fluorescence signals, which originate from the entire volume. Based on the simulation, we estimate the ratio of effective interrogation volumes of photocurrent to photoluminescence detection to be the order of 1:20.

## Future perspectives

Understanding physical processes and dependency of external electromagnetic fields and defect concentrations within the crystal constitutes a fundamental aspect in the development of advanced quantum sensors, pulse sequence design, and determination of the effects of the crystal environment. Describing the recombination mechanism occurring at the electrode/crystal boundary or in proximity to the surface can explain phenomena such as high PDMR contrast, where observed PDMR contrast may exceed 50% or the dependency of the NV charge state flipping with the applied bias voltage. The calculated quantum efficiency is important in optimizing the pulse protocol to increase the efficiency of electrical readout and its dependency on the  $N_s$  defect concentration. Leveraging the COMSOL-MatLab interface facilitates direct examination of output signals in newly designed chip/electrode configurations. Furthermore, the utilization of microwave-free GSLAC-assisted readout chip sensors enables the deployment of diamond-based quantum sensors in biological systems, circumventing the need for microwave exposure. Coupled with precise modelling, this approach aids in determining crystal thickness and doping profiles to maximise the efficacy of photoelectrical readout via GSLAC.

## 5.3 Chip design and testing

Two chips were developed and fabricated: one tailored for single crystal diamond and another for sensing via nanodiamond particles. Designs for both chips were optimized for microwave field distribution and potential resonance patterns. Single crystal diamond chips employed a tri-plate configuration engineered to achieve a homogenous magnetic part of the microwave field intensity surrounding the laser aperture, aligned parallel to the z-axis of the model. S-parameters within the frequency range exhibited flat characteristics, and no resonance pattern was present. Unique electrodes were designed to mitigate microwave interference with the detected photocurrent signal. Chip microwave pickup was modelled, demonstrating minimal interference on the electrode lines (-40 and -50dB). Chip evaluation for the microwave-involved pickup revealed a consistently flat response across different focal points within the frequency range, outperforming currently used chips at the UHasselt group. Moreover, the chip demonstrated promise as a candidate for microfluidic QNMR. An initial prototype was developed and subjected to pulse protocol spin manipulation tests (including Rabi, Ramsay, and Hans Echo). Further optimisation efforts will be focused on refining microwave field

distribution. A quantum chip designed for nanodiamonds was developed to exhibit a resonance pattern around 2.87 GHz. Heating properties were modelled and experimentally validated through temperature sensing by nanodiamonds within an imaging media, which we consider to be a biological phantom. ODMR spectra were acquired, and algorithms successfully detected temperature shifts and Zeeman splitting. Additionally, ODMR spectra were collected from nanodiamond particles attached to the neurons, confirming the retention of Zeeman splitting and thus demonstrating *in vitro* quantum sensing of magnetic fields.

## Future perspectives

The chip developed in this thesis for the single crystal diamond will be tested to measure individual NV defects. The QNMR setup will be upgraded so that one can apply sophisticated pulse sequences to detect NMR signals from aL-pL samples and tune the direction of the main magnetic field. An example of these sequences is XY8 [99]. To detect NMR signals, one can thermally polarize a sample inside a 1.5 T polarization magnet developed at UHasselt group and then transfer the sample as quickly as possible to the microfluidic chip through a high-pressure flow path. Then, the flow will be stopped, and the detection pulse sequence will start. This process will be repeated over and over again until a reasonably good signal-to-noise ratio is achieved. Further setup upgrades can be done by 1) implementing a double resonance pulse sequence [100], 2) Improving the main field uniformity to achieve a 10Hz linewidth resolution. This can be done through an improved design of the magnetic field, e.g., the Halbach array incorporated by gradient fields. 3) Monitoring the temperature of the NMR sample through temperature sensing protocol. 4) Using a CPC lens and light guide to collect as much PL as possible 5) Stabilizing the main magnetic field drift through active monitoring of its magnitude and compensating it by the feedback mechanism. This can be done by installing an auxiliary NV sensor alongside the membrane.

For perspective neuron measurements, we will investigate the dynamics of spontaneous axon growth during development as well as the regenerative plasticity of axonal networks after trauma on diamond-based probes. We will combine the measurement of local temperature gradients using diamond NV centers as a powerful and highly innovative tool for neuroscientific research. Temperature gradients will be defined to represent the skin-to-body core temperature differences (min: 33.5 to max: 37.7 °C) or the differences between healthy and inflamed tissue (~36.6 °C to 42 °C).

## References

- [1] BOURGEOIS, E., A. JARMOLA, P. SIYUSHEV, M. GULKA, J. HRUBY, F. JELEZKO, D. BUDKER a M. NESLADEK. Photoelectric detection of electron spin resonance of nitrogen-vacancy centres in diamond. *Nature Communications* [online]. 2015, **6**(1), 1–8. ISSN 20411723. Dostupné z: doi:10.1038/ncomms9577
- [2] PATAPOUTIAN, Ardem, Andrea M PEIER, Gina M STORY a Veena VISWANATH. ThermoTRP channels and beyond: mechanisms of temperature sensation. *Nature reviews. Neuroscience* [online]. 2003, **4**(7), 529–39. ISSN 1471-003X. Dostupné z: doi:10.1038/nrn1141

- [3] MITA, Yoshimi. Change of absorption spectra in type-I b diamond with heavy neutron irradiation. *Physical Review B* [online]. 1996, **53**(17), 11360–11364. ISSN 0163-1829. Dostupné z: doi:10.1103/PhysRevB.53.11360
- [4] DAVIES G. a HAMER M. F. Optical studies of the 1.945 eV vibronic band in diamond. *Proceedings of the Royal Society of London. A. Mathematical and Physical Sciences* [online]. 1976, **348**(1653), 285–298. ISSN 0080-4630. Dostupné z: doi:10.1098/rspa.1976.0039
- [5] IAKOUBOVSKII, K, G J ADRIAENSSENS a M NESLADEK. Photochromism of vacancy-related centres in diamond. *Journal of Physics: Condensed Matter* [online]. 2000, **12**(2), 189–199. ISSN 0953-8984. Dostupné z: doi:10.1088/0953-8984/12/2/308
- [6] LOUBSER, J.H.N. a J.A. VAN WYK. Optical spin-polarisation in a triplet state in irradiated and annealed type 1b diamonds. In: *Diamond Research*. 1977.
- [7] LOUBSER, J H N a J A van WYK. Electron spin resonance in the study of diamond. *Reports on Progress in Physics* [online]. 1978, **41**(8), 1201–1248. ISSN 0034-4885. Dostupné z: doi:10.1088/0034-4885/41/8/002
- [8] REDMAN, D. A., S. BROWN, R. H. SANDS a S. C. RAND. Spin dynamics and electronic states of N-V centers in diamond by EPR and four-wave-mixing spectroscopy. *Physical Review Letters* [online]. 1991, **67**(24), 3420–3423. ISSN 0031-9007. Dostupné z: doi:10.1103/PhysRevLett.67.3420
- [9] GRUBER, A., A. DRÄBENSTEDT, C. TIETZ, L. FLEURY, J. WRACHTRUP a C. von BORCZYKOWSKI. Scanning Confocal Optical Microscopy and Magnetic Resonance on Single Defect Centers. *Science* [online]. 1997, **276**(5321), 2012–2014. ISSN 0036-8075. Dostupné z: doi:10.1126/science.276.5321.2012
- [10] WOLF, Thomas, Philipp NEUMANN, Kazuo NAKAMURA, Hitoshi SUMIYA, Takeshi OHSHIMA, Junichi ISOYA a Jörg WRACHTRUP. Subpicotesla Diamond Magnetometry. *Physical Review X* [online]. 2015, **5**(4), 041001. ISSN 2160-3308. Dostupné z: doi:10.1103/PhysRevX.5.041001
- [11] NEUMANN, P., I. JAKOBI, F. DOLDE, C. BURK, R. REUTER, G. WALDHERR, J. HONERT, T. WOLF, A. BRUNNER, J. H. SHIM, D. SUTER, H. SUMIYA, J. ISOYA a J. WRACHTRUP. High-Precision Nanoscale Temperature Sensing Using Single Defects in Diamond. *Nano Letters* [online]. 2013, **13**(6), 2738–2742. ISSN 1530-6984. Dostupné z: doi:10.1021/nl401216y
- [12] ACOSTA, Victor Marcel. *Optical Magnetometry with Nitrogen-Vacancy Centers in Diamond*. 2011.
- [13] HE, Xing-Fei, Neil B. MANSON a Peter T. H. FISK. Paramagnetic resonance of photoexcited N- V defects in diamond. II. Hyperfine interaction with the <sup>14</sup>N nucleus. *Physical Review B* [online]. 1993, **47**(14), 8816–8822. ISSN 0163-1829. Dostupné z: doi:10.1103/PhysRevB.47.8816
- [14] GALI, Ádám. Ab initio theory of the nitrogen-vacancy center in diamond. *Nanophotonics* [online]. 2019, **8**(11), 1907–1943 [vid. 2023-02-24]. ISSN 2192-8614. Dostupné z: doi:10.1515/nanoph-2019-0154

- [15] ACOSTA, V. M., E. BAUCH, M. P. LEDBETTER, A. WAXMAN, L.-S. BOUCHARD a D. BUDKER. Temperature Dependence of the Nitrogen-Vacancy Magnetic Resonance in Diamond. *Physical Review Letters* [online]. 2010, **104**(7), 070801. ISSN 0031-9007. Dostupné z: doi:10.1103/PhysRevLett.104.070801
- [16] BARRY, John F., Jennifer M. SCHLOSS, Erik BAUCH, Matthew J. TURNER, Connor A. HART, Linh M. PHAM a Ronald L. WALSWORTH. Sensitivity optimization for NV-diamond magnetometry. *Reviews of Modern Physics* [online]. 2020, **92**(1), 015004 [vid. 2022-09-15]. ISSN 15390756. Dostupné z: doi:10.1103/RevModPhys.92.015004
- [17] WICKENBROCK, Arne, Huijie ZHENG, Lykourgos BOUGAS, Nathan LEEFER, Samer AFACH, Andrey JARMOLA, Victor M. ACOSTA a Dmitry BUDKER. Microwave-free magnetometry with nitrogen-vacancy centers in diamond. *Applied Physics Letters* [online]. 2016, **109**(5), 053505 [vid. 2019-11-15]. ISSN 0003-6951. Dostupné z: doi:10.1063/1.4960171
- [18] ZHENG, Huijie, Zhiyin SUN, Georgios CHATZIDROSOS, Chen ZHANG, Kazuo NAKAMURA, Hitoshi SUMIYA, Takeshi OHSHIMA, Junichi ISOYA, Jörg WRACHTRUP, Arne WICKENBROCK a Dmitry BUDKER. Microwave-Free Vector Magnetometry with Nitrogen-Vacancy Centers along a Single Axis in Diamond. *Physical Review Applied* [online]. 2020, **13**(4), 044023. ISSN 2331-7019. Dostupné z: doi:10.1103/PhysRevApplied.13.044023
- [19] DOHERTY, Marcus W., Viktor V. STRUZHKIN, David A. SIMPSON, Liam P. MCGUINNESS, Yufei MENG, Alastair STACEY, Timothy J. KARLE, Russell J. HEMLEY, Neil B. MANSON, Lloyd C.L. HOLLENBERG a Steven PRAWER. Electronic properties and metrology applications of the diamond NV - Center under pressure. *Physical Review Letters* [online]. 2014. ISSN 00319007. Dostupné z: doi:10.1103/PhysRevLett.112.047601
- [20] PLAKHOTNIK, Taras, Marcus W. DOHERTY, Jared H. COLE, Robert CHAPMAN a Neil B. MANSON. All-optical thermometry and thermal properties of the optically detected spin resonances of the NV- center in nanodiamond. *Nano Letters* [online]. 2014. ISSN 15306992. Dostupné z: doi:10.1021/nl501841d
- [21] BARRY, John F., Jennifer M. SCHLOSS, Erik BAUCH, Matthew J. TURNER, Connor A. HART, Linh M. PHAM a Ronald L. WALSWORTH. Sensitivity optimization for NV-diamond magnetometry. *Reviews of Modern Physics* [online]. 2020, **92**(1), 015004. ISSN 15390756. Dostupné z: doi:10.1103/RevModPhys.92.015004
- [22] MAMIN, H. J., M. KIM, M. H. SHERWOOD, C. T. RETTNER, K. OHNO, D. D. AWSCHALOM a D. RUGAR. Nanoscale Nuclear Magnetic Resonance with a Nitrogen-Vacancy Spin Sensor. *Science* [online]. 2013, **339**(6119), 557–560. ISSN 0036-8075. Dostupné z: doi:10.1126/science.1231540
- [23] GROTZ, Bernhard, Johannes BECK, Philipp NEUMANN, Boris NAYDENOV, Rolf REUTER, Friedemann REINHARD, Fedor JELEZKO, Jörg WRACHTRUP, David SCHWEINFURTH, Biprajit SARKAR a Philip HEMMER. Sensing external spins with nitrogen-vacancy diamond. *New Journal of Physics* [online]. 2011, **13**(5), 055004. ISSN 1367-2630. Dostupné z: doi:10.1088/1367-2630/13/5/055004
- [24] PERUNICIC, V. S., C. D. HILL, L. T. HALL a L. C.L. HOLLENBERG. A quantum spin-probe molecular microscope. *Nature Communications* [online]. 2016, **7** [vid. 2019-11-14]. ISSN 20411723. Dostupné z: doi:10.1038/ncomms12667

- [25] SEGAWA, Takuya F. a Ryuji IGARASHI. Nanoscale quantum sensing with Nitrogen-Vacancy centers in nanodiamonds – A magnetic resonance perspective. *Progress in Nuclear Magnetic Resonance Spectroscopy* [online]. 2023, **134–135**, 20–38. ISSN 00796565. Dostupné z: doi:10.1016/j.pnmrs.2022.12.001
- [26] MOHAN, Nitin, Chao Sheng CHEN, Hsiao Han HSIEH, Yi Chun WU a Huan Cheng CHANG. In vivo imaging and toxicity assessments of fluorescent nanodiamonds in *Caenorhabditis elegans*. *Nano Letters* [online]. 2010, **10(9)**, 3692–3699 [vid. 2024-02-05]. ISSN 15306984. Dostupné z: doi:10.1021/NL1021909/SUPPL\_FILE/NL1021909\_SI\_002.AVI
- [27] SU, Long Jyun, Meng Shiue WU, Yuen Yung HUI, Be Ming CHANG, Lei PAN, Pei Chen HSU, Yit Tsong CHEN, Hong Nerng HO, Yen Hua HUANG, Thai Yen LING, Hsao Hsun HSU a Huan Cheng CHANG. Fluorescent nanodiamonds enable quantitative tracking of human mesenchymal stem cells in miniature pigs. *Scientific Reports 2017 7:1* [online]. 2017, **7(1)**, 1–11 [vid. 2024-02-05]. ISSN 2045-2322. Dostupné z: doi:10.1038/srep45607
- [28] YOSHINO, Fumi, Tsukuru AMANO, Yajuan ZOU, Jian XU, Fuminori KIMURA, Yoshio FURUSHO, Tokuhiro CHANO, Takashi MURAKAMI, Li ZHAO a Naoki KOMATSU. Preferential Tumor Accumulation of Polyglycerol Functionalized Nanodiamond Conjugated with Cyanine Dye Leading to Near-Infrared Fluorescence In Vivo Tumor Imaging. *Small (Weinheim an der Bergstrasse, Germany)* [online]. 2019, **15(48)** [vid. 2024-02-05]. ISSN 1613-6829. Dostupné z: doi:10.1002/SMLL.201901930
- [29] ZHANG, Kuikui, Qi ZHAO, Shirong QIN, Yang FU, Runze LIU, Jinfang ZHI a Chongxin SHAN. Nanodiamonds conjugated upconversion nanoparticles for bio-imaging and drug delivery. *Journal of Colloid and Interface Science* [online]. 2019, **537**, 316–324 [vid. 2024-02-05]. ISSN 0021-9797. Dostupné z: doi:10.1016/J.JCIS.2018.11.028
- [30] WEI, Shiguo, Lin LI, Xiangbin DU a Yingqi LI. OFF–ON nanodiamond drug platform for targeted cancer imaging and therapy. *Journal of Materials Chemistry B* [online]. 2019, **7(21)**, 3390–3402 [vid. 2024-02-05]. ISSN 2050-7518. Dostupné z: doi:10.1039/C9TB00447E
- [31] MOCHALIN, Vadym N., Olga SHENDEROVA, Dean HO a Yury GOGOTSI. The properties and applications of nanodiamonds. *Nature Nanotechnology* [online]. 2012, **7(1)**, 11–23. ISSN 1748-3387. Dostupné z: doi:10.1038/nnano.2011.209
- [32] NEUMANN, P., I. JAKOBI, F. DOLDE, C. BURK, R. REUTER, G. WALDHERR, J. HONERT, T. WOLF, A. BRUNNER, J. H. SHIM, D. SUTER, H. SUMIYA, J. ISOYA a J. WRACHTRUP. High-precision nanoscale temperature sensing using single defects in diamond. *Nano Letters* [online]. 2013. ISSN 15306984. Dostupné z: doi:10.1021/nl401216y
- [33] CHOE, Sunuk, Jungbae YOON, Myeongwon LEE, Jooeon OH, Dongkwon LEE, Heeseong KANG, Chul-Ho LEE a Donghun LEE. Precise temperature sensing with nanoscale thermal sensors based on diamond NV centers. *Current Applied Physics* [online]. 2018, **18(9)**, 1066–1070. ISSN 15671739. Dostupné z: doi:10.1016/j.cap.2018.06.002
- [34] PETRINI, Giulia, Giulia TOMAGRA, Ettore BERNARDI, Ekaterina MOREVA, Paolo TRAINA, Andrea MARCANTONI, Federico PICOLLO, Klaudia KVAKOVÁ, Petr CÍGLER, Ivo Pietro DEGIOVANNI, Valentina CARABELLI a Marco GENOVESE. Nanodiamond–Quantum Sensors Reveal Temperature Variation Associated to Hippocampal Neurons Firing.

- Advanced Science* [online]. 2022, **9**(28), 2202014 [vid. 2024-02-05]. ISSN 2198-3844. Dostupné z: doi:10.1002/ADVS.202202014
- [35] WIRTITSCH, D., G. WACHTER, S. REISENBAUER, M. GULKA, V. IVÁDY, F. JELEZKO, A. GALI, M. NESLADEK a M. TRUPKE. Exploiting ionization dynamics in the nitrogen vacancy center for rapid, high-contrast spin, and charge state initialization. *Physical Review Research* [online]. 2023, **5**(1), 013014 [vid. 2023-02-22]. ISSN 26431564. Dostupné z: doi:10.1103/PhysRevResearch.5.013014
- [36] BOURGEOIS, Emilie, Michal GULKA a Milos NESLADEK. Photoelectric Detection and Quantum Readout of Nitrogen-Vacancy Center Spin States in Diamond. *Advanced Optical Materials* [online]. 2020, **8**(12), 1902132 [vid. 2022-09-15]. ISSN 2195-1071. Dostupné z: doi:10.1002/ADOM.201902132
- [37] BOURGEOIS, E., E. LONDERO, K. BUCZAK, J. HRUBY, M. GULKA, Y. BALASUBRAMANIAM, G. WACHTER, J. STURSA, K. DOBES, F. AUMAYR, M. TRUPKE, A. GALI a M. NESLADEK. Enhanced photoelectric detection of NV magnetic resonances in diamond under dual-beam excitation. *Physical Review B* [online]. 2017, **95**(4), 041402 [vid. 2022-09-16]. ISSN 24699969. Dostupné z: doi:10.1103/PhysRevB.95.041402
- [38] HRUBY, Jaroslav, Michal GULKA, Massimo MONGILLO, Iuliana P. RADU, Michael V. PETROV, Emilie BOURGEOIS a Milos NESLADEK. Magnetic field sensitivity of the photoelectrically read nitrogen-vacancy centers in diamond. *Applied Physics Letters* [online]. 2022, **120**(16), 162402 [vid. 2022-09-15]. ISSN 0003-6951. Dostupné z: doi:10.1063/5.0079667
- [39] BOURGEOIS, Emilie, Josef SOUCEK, Jaroslav HRUBY, Michal GULKA a Milos NESLADEK. Photoelectric Detection of Nitrogen-Vacancy Centers Magnetic Resonances in Diamond: Role of Charge Exchanges with Other Optoelectrically Active Defects. *Advanced Quantum Technologies* [online]. 2022, **5**(5), 2100153 [vid. 2022-09-16]. ISSN 25119044. Dostupné z: doi:10.1002/qute.202100153
- [40] BOURGEOIS, Emilie, Michal GULKA a Milos NESLADEK. Photoelectric Detection and Quantum Readout of Nitrogen-Vacancy Center Spin States in Diamond. *Advanced Optical Materials* [online]. 2020, **8**(12), 1902132. ISSN 2195-1071. Dostupné z: doi:10.1002/ADOM.201902132
- [41] LIN, Web-Chieh a Gary FEDDER. A Comparison of Induction-Detection NMR and Force Detection NMR on Micro-NMR Device Design. 2001.
- [42] BUCHER, Dominik B., Diana P. L. AUDE CRAIK, Mikael P. BACKLUND, Matthew J. TURNER, Oren BEN DOR, David R. GLENN a Ronald L. WALSWORTH. Quantum diamond spectrometer for nanoscale NMR and ESR spectroscopy. *Nature Protocols* [online]. 2019, **14**(9), 2707–2747. ISSN 1754-2189. Dostupné z: doi:10.1038/s41596-019-0201-3
- [43] SAID, Tarek a Vasundara V. VARADAN. Variation of Cole-Cole model parameters with the complex permittivity of biological tissues. In: *2009 IEEE MTT-S International Microwave Symposium Digest* [online]. B.m.: IEEE, 2009, s. 1445–1448. ISBN 978-1-4244-2803-8. Dostupné z: doi:10.1109/MWSYM.2009.5165979
- [44] ROBLEDO, Lucio, Hannes BERNIEN, Toeno Van Der SAR a Ronald HANSON. Spin dynamics in the optical cycle of single nitrogen-vacancy centres in diamond. *New Journal of*

- Physics* [online]. 2011, **13**(2), 025013 [vid. 2023-06-19]. ISSN 1367-2630. Dostupné z: doi:10.1088/1367-2630/13/2/025013
- [45] BOURGEOIS, E., A. JARMOLA, P. SIYUSHEV, M. GULKA, J. HRUBY, F. JELEZKO, D. BUDKER a M. NESLADEK. Photoelectric detection of electron spin resonance of nitrogen-vacancy centres in diamond. *Nature Communications* [online]. 2015, **6**(1), 1–8 [vid. 2022-09-15]. ISSN 20411723. Dostupné z: doi:10.1038/ncomms9577
- [46] TETIENNE, J. P., L. RONDIN, P. SPINICELLI, M. CHIPAUX, T. DEBUISSCHERT, J. F. ROCH a V. JACQUES. Magnetic-field-dependent photodynamics of single NV defects in diamond: Application to qualitative all-optical magnetic imaging. *New Journal of Physics* [online]. 2012, **14** [vid. 2022-09-23]. ISSN 13672630. Dostupné z: doi:10.48550/arxiv.1206.1201
- [47] MUROOKA, T., M. SHIIGAI, Y. HIRONAKA, T. TSUJI, B. YANG, T. M. HOANG, K. SUDA, K. MIZUNO, H. KATO, T. MAKINO, M. OGURA, S. YAMASAKI, M. HATANO a T. IWASAKI. Photoelectrical detection of nitrogen-vacancy centers by utilizing diamond lateral p–i–n diodes. *Applied Physics Letters* [online]. 2021, **118**(25), 253502 [vid. 2022-09-15]. ISSN 0003-6951. Dostupné z: doi:10.1063/5.0055852
- [48] SIYUSHEV, Petr, Milos NESLADEK, Emilie BOURGEOIS, Michal GULKA, Jaroslav HRUBY, Takashi YAMAMOTO, Michael TRUPKE, Tokuyuki TERAJI, Junichi ISOYA a Fedor JELEZKO. Photoelectrical imaging and coherent spin-state readout of single nitrogen-vacancy centers in diamond. *Science* [online]. 2019, **363**(6428), 728–731 [vid. 2019-11-19]. ISSN 10959203. Dostupné z: <https://www.science.org/doi/10.1126/science.aav2789>
- [49] MALINAUSKAS, T., K. JARAŠIŪNAS, E. IVAKIN, N. TRANCHANT a M. NESLADEK. Determination of carrier diffusion coefficient and lifetime in single crystalline CVD diamonds by light-induced transient grating technique. *physica status solidi (a)* [online]. 2010, **207**(9), 2058–2063 [vid. 2024-01-25]. ISSN 1862-6319. Dostupné z: doi:10.1002/PSSA.201000100
- [50] RADKO, Ilya P., Mads BOLL, Niels M. ISRAELSEN, Nicole RAATZ, Jan MEIJER, Fedor JELEZKO, Ulrik L. ANDERSEN a Alexander HUCK. Determining the internal quantum efficiency of shallow-implanted nitrogen-vacancy defects in bulk diamond. *Optics Express* [online]. 2016, **24**(24), 27715 [vid. 2022-09-16]. ISSN 10944087. Dostupné z: doi:10.1364/OE.24.027715
- [51] SMITS, Janis, Joshua T. DAMRON, Pauli KEHAYIAS, Andrew F. MCDOWELL, Nazanin MOSAVIAN, Ilja FESCENKO, Nathaniel RISTOFF, Abdelghani LARAOUI, Andrey JARMOLA a Victor M. ACOSTA. Two-dimensional nuclear magnetic resonance spectroscopy with a microfluidic diamond quantum sensor. *Science Advances* [online]. 2019, **5**(7). ISSN 2375-2548. Dostupné z: doi:10.1126/sciadv.aaw7895
- [52] GRANDINETTI, Philip J., Jason T. ASH a Nicole M. TREASE. Symmetry pathways in solid-state NMR. *Progress in Nuclear Magnetic Resonance Spectroscopy* [online]. 2011, **59**(2), 121–196. ISSN 00796565. Dostupné z: doi:10.1016/j.pnmrs.2010.11.003

## Author relevant publications

{1} - BOURGEOIS, Emilie; SOUCEK, Josef; HRUBY, Jaroslav; GULKA, Michal and NESLADEK, Milos. Photoelectric Detection of Nitrogen-Vacancy Centers Magnetic Resonances in Diamond: Role of Charge Exchanges with Other Optoelectrically Active Defects. Online. *Advanced Quantum Technologies*. 2022, yr. 5, p. 5. ISSN 2511-9044. Available from: <https://doi.org/10.1002/qute.202100153>. [cit. 2024-03-12].

{2} - ZHENG, Huijie; HRUBY, Jaroslav; BOURGEOIS, Emilie; SOUCEK, Josef; SIYUSHEV, Petr et al. Electrical-Readout Microwave-Free Sensing with Diamond. Online. *Physical Review Applied*. 2022, yr. 18, p. 2. ISSN 2331-7019. Available from: <https://doi.org/10.1103/PhysRevApplied.18.024079>. [cit. 2024-03-12].

{3} - SOUCEK, Josef; PETROV, Michael; GULKA, Michal; BOURGEOIS, Emilie; and NESLADEK, Milos. Modelling and experimental verification of photoelectrical response of NV diamond spin-centres. *Physical Review Applied*. 2024, Manuscript under review.

## Other publications

{4} - CHANG, Yu-Ying, Jiří STUHLÍK, Neda NEYKOVA, Josef SOUČEK a Zdeněk REMEŠ. Optical properties of the plasma hydrogenated ZnO thin films. *Journal of Electrical Engineering* [online]. 2017, **68**(7), 70-73 [cit. 2019-09-19]. DOI: 10.1515/jee-2017-0060. ISSN 1339-309X.

{5} - REMES, Z, Y Y CHANG, J STUHLÍK, N NEYKOVA, J SOUCEK a Hua Shu HSU. Enhanced room temperature exciton photoluminescence of plasma hydrogenated ZnO nanocolumns. *IOP Conference Series: Materials Science and Engineering* [online]. 2018, **465** [cit. 2019-09-19]. DOI: 10.1088/1757-899X/465/1/012008

To date citation of author's articles according to Scopus  
- Total citation: 20

## Summary

Recent developments of engineered nitrogen-vacancy (NV) centres in diamonds offer promising avenues for the creation of sensitive nanoscale probes, pivotal for quantum measurements and diagnostic applications in nanomedicine. The aim of this work is to enable these sensor applications by studying NV photodynamics, investigating the effects of the environment and developing advanced quantum sensor chips. In this thesis, we include both fluorescent nanodiamond particles (NDs) and NV-containing single crystal diamond. Initially, we study the fundamental physics governing signal generation, exploring the photodynamics of a single NV center and analysing its spin-contrast properties. Subsequently, we probe the impact of the crystal environment on the photoelectrical signals and quantum efficiency, determining the possible origins of non-standard phenomena such as positive photocurrent detected magnetic resonance (PDMR). We demonstrate the usage of ground-state level anti-crossing (GSLAC) in photoelectrical spin-state readout.

In the second part of the thesis, we focused on the development of a quantum chip for both single-crystal diamond and ND particles. Two types of prototypes were designed and fabricated, with numerical modelling employed to elucidate microwave field distribution and resonance patterns. For single crystal diamond chips, in-depth testing is conducted to mitigate microwave-induced interference, which is critical for detecting low photocurrents from single NV centres. Additionally, we explore the potential for integrating this chip into a microfluidic chamber. The chip for the nanodiamond particles was evaluated for its heating properties, which are crucial for keeping neurons alive, using theoretical calculations and experimental measurements using a nanodiamond probe. Furthermore, we also perform the *in vitro* sensing of the magnetic field at the attached nanodiamonds to the neuron cells.

In summary, our research represents a significant step forward in harnessing the capabilities of engineered NV centers in diamond for quantum sensing applications, offering promising prospects in both fundamental research and practical diagnostics in nanomedicine.

